

ANKARA YILDIRIM BEYAZIT UNIVERSITY

GRADUATE SCHOOL OF NATURAL AND APPLIED SCIENCES



**SPARSE MATRIX DECOMPOSITION AND LOW RANK BASED
TECHNIQUES FOR ANOMALY DETECTION IN
HYPERSPPECTRAL IMAGES**

Ph.D. Thesis by

Fatma KÜÇÜK

Department of Computer Engineering

February, 2020

ANKARA

**SPARSE MATRIX DECOMPOSITION AND LOW RANK
BASED TECHNIQUES FOR ANOMALY DETECTION
IN HYPERSPECTRAL IMAGES**

A Thesis Submitted to

The Graduate School of Natural and Applied Sciences of

Ankara Yıldırım Beyazıt University

**In Partial Fulfillment of the Requirements for the Degree of Doctor of
Philosophy in Computer Engineering, Department of Computer Engineering**

by

Fatma KÜÇÜK

February, 2020

ANKARA

Ph.D. THESIS EXAMINATION RESULT FORM

We have read the thesis entitled “**SPARSE MATRIX DECOMPOSITION AND LOW RANK BASED TECHNIQUES FOR ANOMALY DETECTION IN HYPERSPECTRAL IMAGES**” completed by **FATMA KÜÇÜK** under the supervision of **PROF. DR. FATİH VEHBİ ÇELEBİ** and **ASSOC. PROF. DR. BEHÇET UĞUR TÖREYİN** and we certify that in our opinion it is fully adequate, in scope and in quality, as a thesis for the degree of Doctor of Philosophy.

Prof. Dr. Fatih Vehbi ÇELEBİ

Supervisor

Assoc. Prof. Dr. Behçet Uğur TÖREYİN

Co-Supervisor

Assist. Prof. Dr. Osman Serdar GEDİK

Jury Member

Prof. Dr. Süleyman TOSUN

Jury Member

Assist. Prof. Dr. Fatih NAR

Jury Member

Assist. Prof. Dr. Hilal KAYA

Jury Member

Prof. Dr. Ergün ERASLAN

Director

Graduate School of Natural and Applied Sciences

ETHICAL DECLARATION

I hereby declare that, in this thesis which has been prepared in accordance with the Thesis Writing Manual of Graduate School of Natural and Applied Sciences,

- All data, information and documents are obtained in the framework of academic and ethical rules,
- All information, documents and assessments are presented in accordance with scientific ethics and morals,
- All the materials that have been utilized are fully cited and referenced,
- No change has been made on the utilized materials,
- All the works presented are original,

and in any contrary case of above statements, I accept to renounce all my legal rights.

Date: 13.02.2020

Signature:

Name & Surname: Fatma Küçük

ACKNOWLEDGMENTS

Firstly, I would like to express my sincere gratitude to my supervisors, Prof.Dr. Fatih Vehbi ÇELEBİ and Assoc.Prof.Dr. Behçet Uğur Töreyn for their supports and motivation during my study. I find myself very lucky to work with polite and wise advisors. I would like to thank Assoc.Prof.Dr. Behçet Uğur Töreyn again for taking the time to share his experiences and recommendations and to guide me through my work.

I also would like thank Assist. Prof. Dr. Osman Serdar Gedik, Prof. Dr. Süleyman Tosun, Assist. Prof. Dr. Hilal Kaya and Assist. Prof. Dr. Fatih Nar for their valuable contributions and constructive comments during my thesis monitoring committees, which have improved the quality of the thesis

Finally, I am grateful to my family for supporting me during my Ph.D. study. I would like to thank them for motivating me all the time.

2020, 13 February

Fatma KÜÇÜK

SPARSE MATRIX DECOMPOSITION AND LOW RANK BASED TECHNIQUES FOR ANOMALY DETECTION IN HYPERSPPECTRAL IMAGES

ABSTRACT

Hyperspectral imagery is a popular remote sensing technology to distinguish materials on the ground surface. The reflected and emitted radiation detected by a high number of narrow, contiguous, and continuous spectral bands are collected by imaging spectrometers. They are, then, analyzed, and evaluated by this technology. Hyperspectral image processing techniques have been applied in many application fields with different aims, such as in military for target detection, in agriculture to classify crops, in nourishment to determine the freshness of food, in medicine for detecting diseased areas.

In this study, a sparse and low-rank matrix decomposition-based anomaly detection method for hyperspectral data is proposed. High dimensional data is decomposed into low-rank and sparse matrices representing background and anomalies, respectively. The problem of the decomposition process is defined from the dictionary learning point of view. Therefore, the way of obtaining these matrices differs from previous studies. It aims to find a correct partition of the data and separate anomaly pixels from the background. After decomposition, Mahalanobis Distance is applied to the sparse part of the data in order to get anomaly locations. Experiments are conducted with twenty hyperspectral datasets, in total. Anomaly materials in these images are plane, vehicle, rock, metal sheet, field crop, synthetic data. Experimental results suggest that the anomaly detection performance of the proposed method surpasses those of the state-of-the-art methods above 90% AUC value.

Keywords: Hyperspectral imaging, anomaly detection, low-rank and sparse matrix decomposition.

HİPERSPEKTRAL GÖRÜNTÜLERDE ANOMALİ TESPİTİ İÇİN SEYREK MATRİS AYRIŞTIRMA VE DÜŞÜK SIRALI TEKNİKLER

ÖZ

Hiperspektral görüntüleme, yer yüzeyindeki malzemeleri ayırt etmek için popüler bir uzaktan algılama teknolojisidir. Çok sayıda dar, bitişik ve sürekli spektral bant tarafından saptanan yansıyan ve yayılan radyasyon görüntüleme spektrometreleri ile toplanır. Daha sonra bu teknoloji tarafından analiz edilir ve değerlendirilirler. Hiperspektral görüntü işleme teknikleri, tarımsal bitkileri tespit etmek ve sınıflandırmak, gıdaların tazeliğini belirlemek, tıpta hastalıklı alanları tespit etmek gibi farklı amaçlarla birçok uygulama alanında kullanılmaktadır.

Bu çalışmada, hiperspektral veriler için seyrek ve düşük dereceli bir matris ayrışmasına dayalı anomali saptama yöntemi önerilmiştir. Yüksek boyutlu veriler, sırasıyla arka planı ve anomalileri temsil eden düşük dereceli ve seyrek matrislere ayrıştırılır. Bu ayrıştırma problemi sözlük öğrenme bakış açısıyla tanımlanır. Bu nedenle, bu matrisleri elde etmenin yolu önceki çalışmalardan farklıdır. Verilerin doğru bir bölümünü bulmayı ve anomali piksellerini arka plandan ayırmayı amaçlamaktadır. Ayrıştırma işleminden sonra, verilerin seyrek matris kısmına anomali yerleri bulmak için Mahalanobis uzaklığı uygulanır. Deneysel sonuçlar, önerilen yöntemin anomali saptama performansının, en gelişmiş yöntemlerin performansını aştığını göstermektedir.

Anahtar Kelimeler: Hiperspektral görüntüleme, anomali tespiti, düşük dereceli ve seyrek matris ayrışma.

CONTENTS

Ph.D. THESIS EXAMINATION RESULT FORM	ii
ETHICAL DECLARATION.....	iii
ACKNOWLEDGMENTS	iv
ABSTRACT.....	v
ÖZ.....	vi
NOMENCLATURE	ix
LIST OF TABLES.....	xii
LIST OF FIGURES.....	xiii
CHAPTER 1 - INTRODUCTION.....	1
1.1 Problem Statement and Motivation	2
1.2 Contributions of the Thesis	3
1.3 Outline of the Thesis.....	4
CHAPTER 2 - BACKGROUND	5
2.1 Hyperspectral Imagery.....	5
2.2 Literature Review	6
2.2.1 Target Detection	6
2.2.2 Anomaly Detection	7
2.2.3 Matrix Decomposition Based Anomaly Detection	9
CHAPTER 3 - METHODOLOGY.....	12
3.1 Proposed Method.....	13
3.2 Selected Methods	15
3.2.1 RX Anomaly Detector.....	15
3.2.2 SSRX Anomaly Detector.....	16
3.2.3 LRaSMD Anomaly Detector	16
3.2.4 LSMAD Anomaly Detector	17
CHAPTER 4 - HYPERSPECTRAL DATASETS.....	19
4.1 San Diego Airport.....	19
4.2 Cri.....	21
4.3 Pavia Centre	21
4.4 Pavia University	22

4.5 Salinas.....	24
4.6 Indian Pines.....	27
4.7 Airport Beach Urban Data	29
CHAPTER 5 - EXPERIMENTAL RESULTS	32
5.1 Experimental Setup	32
5.2 Experimental Results	32
5.3 Performance Analysis	37
CHAPTER 6 - CONCLUSION	46
REFERENCES	47
CURRICULUM VITAE	56

NOMENCLATURE

Roman Letter Symbols

B	Background matrix
D	Distance
\mathcal{D}	Observed Data
E	Eigen vector
k	Cardinality
L	Low-rank matrix
W	Block diagonal matrix
N	Number of total pixels
r	Rank
\mathcal{R}	Real numbers
S	Anomaly matrix
S_i	Subspaces
X	Hyperspectral image data
X_i	Band image vector
V	Eigen vector
Y	Lagrange multiplier

Greek Letter Symbols

λ	Regularization parameter
Σ	Eigen value
ε	Error tolerance
γ_1	Threshold parameter
γ_2	Threshold parameter
λ_i	Eigen values
μ_t	Lagrange multiplier
μ	Mean
Γ	Covariance
τ_o	Threshold operator

Subscripts

b	Band Number
F	Frobenius norm
h	Height
i	Index
min	Minimum
n	Number of total pixels
w	Weight

Acronyms

ABU	Airport Beach Urban
ACE	Adaptive Cosine/Coherent Estimator
AMSD	Adaptive Matched Subspace Detector
AVIRIS	Airborne Visible/Infrared Imaging Spectrometer
CBAD	Cluster Based Anomaly Detector
CEM	Constraint Energy Minimization
ENVI	Environment for Visualizing Images
FAR	False Alarm Rate
FN	False Negative
FP	False Positive
FPR	False Positive Rate
GLRT	Generalized Likelihood Ratio Test
GoDec	Go Decomposition
GRX	Global RX
HSI	Hyperspectral Image
KASD	Kernel Adaptive Subspace Detector
KRX	Kernel RX
LADM	Linearized Alternating Direction Method
LLEAD	Locally Linear Embedding Anomaly Detector
LRaSMD	Low-Rank and Sparse Matrix Decomposition
LRR	Low-Rank Representation
LRX	Local RX
LSMAD	Low-Rank and Sparse Matrix Decomposition based Anomaly Detection
MF	Matched Filter

Pd	Probability of Detection
Pfa	Probability of False Alarm
RGB	Red Green Blue
ROSIS	Reflective Optics System Imaging Spectrometer
RX	Reed Xiaoli
RXD	RX Detector
RoSuRe	Robust Subspace Recovery
OSP	Orthogonal Subspace Projection
PaviaC	Pavia Centre
PaviaU	Pavia University
Pd	Probability of Detection
Pfa	Probability of false alarm
PUT	Pixel Under Test
ROC	Receiver Operating Characteristic
SAM	Spectral Angle Mapper
SDA	San Diego Airport
SSC	Sparse Subspace Clustering
SLRMD	Sparse and Low-Rank Matrix Decomposition
SSRX	Subspace RX
SVDD	Support Vector Data Description
TN	True Negative
TP	True Positive
TPR	True Positive Rate

LIST OF TABLES

Table 5.1 AUC values of the methods for hyperspectral datasets	39
Table 5.2 AUC values for the datasets according to materials.....	40

LIST OF FIGURES

Figure 2.1 Principle of imaging spectroscopy	5
Figure 2.2 An example of hyperspectral data cube, and an image at a single band from that data	6
Figure 2.3 X is the observed data, L is the background, and S is the anomalies.....	8
Figure 4.1 SDA RGB image.....	19
Figure 4.2 SDA subset 1 (a) band image. (b) ground truth.	20
Figure 4.3 SDA subset 2 (a) band image. (b) ground truth.	20
Figure 4.4 SDA subset 3 (a) band image. (b) subset1 band image.....	20
Figure 4.5 Cri image. (a) band image. (b) ground truth.	21
Figure 4.6 PaviaC RGB image.	21
Figure 4.7 PaviaC subset. (a)band image. (b)ground truth.....	22
Figure 4.8 PaviaU RGB image..	22
Figure 4.9 PaviaU. (a) band image. (b) ground truth classes. (c) classes with fields.. ..	23
Figure 4.10 PaviaU. (a) Sample 5 band image. (b) ground truth.....	24
Figure 4.11 Salinas. (a) band image. (b) ground truth classes. (c) classes with fields.. ..	25
Figure 4.12 Salinas Real. (a) band image. (b) ground truth..	26
Figure 4.13 Salinas synthetic data. (a) band image. (b) ground truth.	26
Figure 4.14 Indian Pines. (a) band image. (b) ground truth classes. (c) classes with fields.....	27
Figure 4.15 Indian Pines (a) Classes. (b) Sample 1. (c) Sample 2. (d) Sample 3. (e) Sample 4. (f) Sample 5.....	28
Figure 4.16 ABU airport 1. (a) band image. (b) ground truth.....	29
Figure 4.17 ABU airport 2. (a) band image. (b) ground truth.	29
Figure 4.18 ABU airport 4. (a) band image. (b) ground truth.....	30
Figure 4.19 ABU urban 3. (a) band image. (b) ground truth	30
Figure 4.20 ABU urban 4. (a) band image. (b) ground truth	31
Figure 4.21 ABU urban 5. (a) band image. (b) ground truth.....	31
Figure 5.1 Two-dimensional results for the a) SDA subset 1.b) SDA subset 2. c) SDA subset3. d) Cri. e) PaviaC. f) PaviaU sample 5. g) Salinas real. h) Salinas imp4. i) Salinas imp14. j) Indian Pines sample 1. k) Indian Pines sample 2. l) Indian Pines sample 3. m) Indian Pines sample 4. n) Indian Pines sample 5. o) ABU airport 1. p)	

ABU airport 2. q) ABU airport 3. r) ABU urban 3. s) ABU urban 4. t) ABU urban 5.
(a) SLRMD. (b) LSMAD. (c) LRSMD. (d) SSRX. (e) GRX.....34

Figure 5.2 ROC curves for a) SDA subset 1. b) SDA subset 2. c) Cri d) PaviaC. e)
PaviaU sample 5. f) Salinas real. g) Salinas imp4. h) Salinas imp14. i) Indian Pines
sample 1. j) Indian Pines sample 2. k) Indian Pines sample 3. l) Indian Pines sample 4.
m) Indian Pines sample 5. n) ABU airport 1. o) ABU airport 2. p) ABU airport 4. q)
ABU urban 3. r) ABU urban 4. s) ABU urban 5.42

CHAPTER 1

INTRODUCTION

Hyperspectral image processing is a popular remote sensing technology to differentiate materials on the ground surface. It is a passive sensor that uses the environment light, i.e. due to sun. The reflected and emitted radiation detected by large number of narrow, and continuous spectral bands are gathered by the spectrometers. The spectral bands are, then, processed and evaluated by this technology. Hyperspectral image processing methods have been used in different types of applications with different purposes, as in military for target detection, agriculture for classification of crops, nourishment to determine the freshness of food, and medicine for identifying infected regions [1–3].

Hyperspectral imagery collects and processes information from the electromagnetic spectrum. While the human eye can see visible lights in three bands; red, green, and blue, hyperspectral imaging allow one to divide the spectrum into hundreds of bands. A set of images is collected by the hyperspectral sensors. These types of images are three-dimensional data cubes which they hold the spatial and spectral information of them. Apart from having each pixel information in image scene, hyperspectral data holds unique spectral signature information for each pixel. Spectral signatures of hundreds of materials have been processed. They are hold in the spectral libraries. These libraries have been used to identify the materials in hyperspectral image (HSI) data. In other words, spectral signatures can be processed for material detection, classification, identification, and characterization.

One of the advantages of hyperspectral technology is holding the spectrum information. It also takes the advantage of having spatial information. These advantages allow more effective detection and classification methods to be built. The disadvantage of the technology is the cost and complexity. It generally needs high data storage capability. It requires the computer with higher performance to process the HSI data. These needs increase the cost of the technology.

In this chapter, brief information about hyperspectral imagery is firstly given. Then, the problem statement and motivation of the thesis are clarified. It is followed by the contributions of the thesis. Lastly, the outline of the study is presented.

1.1 Problem Statement and Motivation

Hyperspectral sensors can store both spectral and spatial information of a scene in hyperspectral data. With this known information, it is possible to detect targets or objects of interest in an image [4]. This type of detection is entitled hyperspectral target detection [5, 6]. It is a binary classification problem, and a supervised algorithm which can be used to divide pixels into two groups, as a member of a target class or a non-target class, using the spectral information of the target material under consideration, in advance [7]. However, having spectral signature information of any possible target material is not always available and easy. Atmospheric affects, cloud shadows etc. change the observed spectral signature in the image. Pure spectra obtained from the laboratory measurements are hardly observed in the image.

For this reason, unsupervised target detection techniques, which are also referred as anomaly detection methods, can be considered as an alternative to target detection techniques, and take attention in many hyperspectral applications [8, 9]. The basic purpose of anomaly detection techniques is to determine unusual pixels from the background without having any prior information about the target and background.

In this study, a Sparse and Low-Rank Matrix Decomposition based anomaly detection (SLRMD) method is introduced [10]. Linearized Alternating Direction Method (LADM) based Robust Subspace Recovery via Bi-sparsity (RoSuRe) algorithm is applied for decomposing high dimensional hyperspectral data as low-rank and sparse matrices [11,12]. In contrast with the SLRMD method, the RoSuRe method is substantially developed for video background estimation and face clustering problems on RGB data [13]. Authors propose to subtract the background from the foreground which includes moving objects as outliers. The method is compared with Low-Rank Representation (LRR) and Sparse Subspace Clustering (SSC) methods for face clustering problem [14, 15]. It is shown that bi-sparsity model is an effective method

for eliminating sparse errors from high dimensional data. According to its effective results on RGB data and being suitable for high dimensional data, this algorithm is applied to hyperspectral images aiming for determining anomalies. Furthermore, the anomalies in an image can be considered sparse consisting of less number of pixel. In addition, sparse models can be applied for hyperspectral images as a result of being small size and having low probabilities. Based on the above considerations and being convenient with hyperspectral imagery, the idea of decomposing high dimensional data as a sum of low-rank background and sparse anomaly matrices is appropriate for hyperspectral images [16]. Thus, a Low-Rank and Sparse Matrix Decomposition (LRaSMD) based anomaly detection method is proposed in this study [17].

1.2 Contributions of the Thesis

The contribution of the study can be identified in the followings. The proposed method eliminates anomalies from the background effectively compared to the other anomaly detectors, in which they must first model the background, and, then, they can detect the anomalies. In addition, proposed methodology tries to prevent the anomaly statistic map being contaminated with the background information, since the anomaly detector is built by the sparse part of the data. On the contrary, the state-of-the-art anomaly detectors do not have a pure statistical representation of anomaly pixels.

One of the applications of hyperspectral imagery is the target detection. It can be divided into two categories as supervised and unsupervised based algorithms. In supervised perspective, spectral signature of the target is known. As for unsupervised one, spectral signature of the targets is unknown. This type of detection is called anomaly detection. From this point of view, no prior information is needed in anomaly detection methods while spectral signature of the target material is essential and must be known in advance in target detection methods. With this known information, target pixels are searched in the data. As for anomaly detection, the process is to search for inconsistent pixels over all image data. In other words, a priori information (or assumptions) is not used, i.e. statistical modeling of background in anomaly detection. This makes more difficult to detect the anomaly pixels due to containing anomaly pixels in background.

In this study, we intent to propose an anomaly detector based on the matrix decomposition algorithms enabling to decompose data and to obtain anomaly locations. Different from previous LRaSMD based methods, the problem of decomposing data is modeled from the dictionary learning point of view [16–21]. Being motivated by these purposes, the Lagrange function of the optimization problem mentioned in Chapter 3 is expressed as stated in [22]. A sparse matrix is, then, obtained by solving this function, and Mahalanobis Distance is applied to this sparse matrix to retrieve the anomaly locations. By this way, anomalies are separated from their backgrounds.

1.3 Outline of the Thesis

The thesis is organized in six chapters as follows. Chapter 1 introduces the research problem, motivation, and contributions of the thesis. Chapter 2 is the background section. Chapter 3 describes the proposed method in detail. Then, it is followed by the data used for evaluations in Chapter 4. Chapter 5 gives information about the performance results. Finally, the conclusion of the paper is presented in Chapter 6.

CHAPTER 2

BACKGROUND

2.1 Hyperspectral Imagery

Hyperspectral imaging known as imaging spectroscopy is a popular remote sensing technology which supplies information about the materials on the Earth to distinguish and classify them. The reflected and emitted radiation detected by large number of narrow, contiguous and continuous spectral bands are collected by imaging spectrometers. The spectral bands are, then, analyzed, and evaluated by this technology. Imaging spectrometers are defined as the simultaneous acquisition of images in many narrow, contiguous spectral bands [23]. Figure 2.1 is a diagram shows the principle of the imaging spectroscopy.

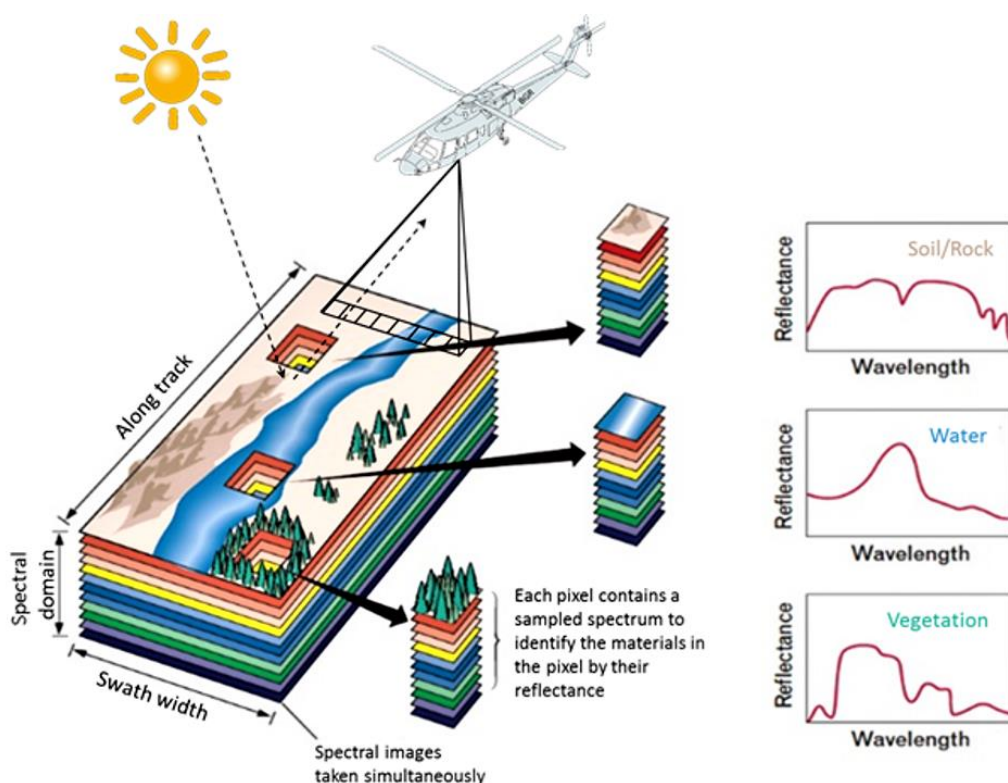


Figure 2.1 Principle of imaging spectroscopy [24].

Hyperspectral imaging systems acquire images in over hundreds of spectral bands. This technology allows identifying and characterizing materials. In addition to mapping distribution of materials, assessment of individual pixels is often useful for detecting unique objects in the scene. In other words, each material has a unique spectral signature, which allows differentiating the materials. For example, soil, water, and vegetation's spectral signatures are distinctly different from each other as seen from Figure 2.1. In addition, an example of hyperspectral data cube and an image at a single band from that data is seen in Figure 2.2. An HSI data cube is consisted from a pile of images in which spatial coordinates for the images at a single band and third coordinate is spectral dimension which gives information about how many numbers of images there are in the dataset. This information is summarized in Figure 2.2.

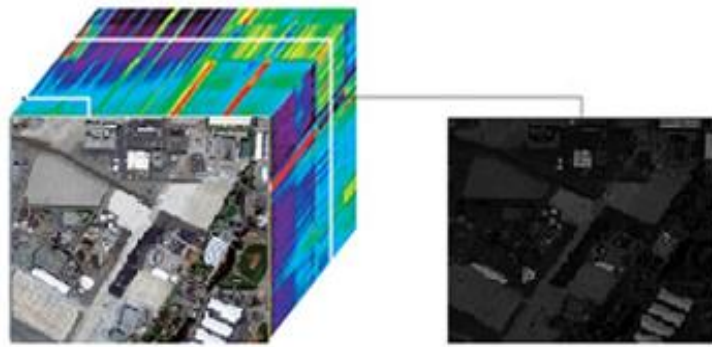


Figure 2.2 An example of hyperspectral data cube, and an image at a single band taken from that data.

2.2 Literature Review

In this section, hyperspectral detection algorithms in the literature are investigated in detail. A well-known application of the hyperspectral imagery is the detection of the objects on the ground surface. They can be categorized with the three main parts.

2.2.1 Target Detection

Target detection is a binary classification process with the aim of labeling every pixel in the image as a target or background. The detection and identification processes of the spectral signature of a known target can be obtained from a spectral library. That is, the target detection which acts as a supervised manner. The most known

hyperspectral target detection algorithms, are Spectral Angle Mapper (SAM) [25], Orthogonal Subspace Projection (OSP) [26], Constraint Energy Minimization (CEM) [27], Generalized Likelihood Ratio Test (GLRT) [28], Adaptive Cosine/Coherent Estimator (ACE) [29], Matched Filter (MF) [30] and Adaptive Matched Subspace Detector (AMSD) [31]. SAM calculates the cosine of the angle between two spectra, the test and the target spectra, aiming to determine spectral similarity between them. The advantage is that it is not affected by pixel brightness. However, hyperspectral data cannot be characterized by the only spectral angle. OSP algorithm is based on linear mixing model which requires whole information about image endmembers. Due to being unrealistic to obtain the complete information, CEM was developed in which only the desired information of endmember is needed. By comparison OSP and CEM, CEM has better results, nonetheless, OSP results can be improved by applying whitening process [32]. GLRT, ACE, and AMSD are the adaptive detectors [33]. AMSD is based on the covariance of the data which is estimated by a training dataset [34]. Among them, ACE has the lowest false alarm rates, but the rate for the methods is affected by not only a big change but also a small change in the value of the threshold [35].

In addition to above mentioned techniques, nonlinear versions of them are also used for the target detection which are called as kernel-based approaches [36-38]. According to the experimental results in the literature, kernel versions of these method performances are better than their linear versions.

2.2.2 Anomaly Detection

Anomaly detection is a process of detecting materials whose spectral signatures stand out from the cluttered background. Any material to be named as an anomaly, their spectral signatures must be distinct from their background pixels. So, there is no prior information of the target is used or needed in these types of methods. They are also adopted when the target information is unreliable. To achieve anomaly detection, the researchers adopt several methods relevant to different disciplines: Statistic based, Kernel based, and Segmentation based anomaly detectors [39].

In this part, statistic-based anomaly detectors are mentioned. The widely used anomaly detection methods primarily obtain information from the background. They subtract the anomalies from the background in order to separate them [40]. Various anomaly detection approaches have been offered and used so far. The well-known one is Reed-Xiaoli (RX) anomaly detection method which is introduced by Reed and Yu [41], and it is constructed from GLRT. Global RX (GRX) or RX uses entire image to estimate background statistic. However, Local RX (LRX) [42], only estimates the background statistics with pixels between two windows around pixel under test (PUT). Subspace RX (SSRX) is introduced later by Schaum [43]. These techniques may be useful in homogeneous areas, but they can be unreliable when the background is comprised of rare and large spectral contaminations. In addition, whole pixels in a local region or in a complete image are utilized to compute the background statistics. Thus, the mean and the covariance matrix of the background are sensitive to corruptions by the anomalies [44, 45], which can minimize the distinction within the anomalies and the background. Yet, there is also the inverse covariance matrix issue, which usually leads to an improper estimation, particularly when it is predicted from a local image. The well-known anomaly detection method is RX detector (RXD) which originates as a GLRT designed to detect a signal of unknown spectral distribution in a data. RXD finds the anomalies which spectrally distinct from the image background. The major problem with statistic-based anomaly detectors is the assumption of the linearity at the background. In fact, the distribution of the probability density function of hyperspectral images is far away from the normal distribution.

Kernel version of anomaly detectors is available which is a modified version of them obtained by kernel functions. They can be called nonlinear anomaly detectors as well. The nonlinear model of the RX method named as kernel RX (KRX) was proposed by Heesung and Nasrabadi [46]. The method is based on its kernelization in the feature space in terms of kernels that computes dot products in the feature space. To estimate the kernel matrix, properties of the kernel principal component analysis are used. Kwon and Nasrabadi in [47] proposed Kernel Adaptive Subspace Detector (KASD) where data is represented with a nonlinear Gaussian RBF kernel function. Another method is Support Vector Data Description (SVDD) [48]. The problem arisen with

kernel version of the anomaly detectors is the determination of the scaling parameter sigma when RBF kernel is used. Another concern is to determine threshold automatically.

Segmentation based anomaly detector are built to overcome the effect of homogeneity of the background on the increasing false alarm rate. Cluster Based Anomaly Detector (CBAD) is a benchmark anomaly detector for segmentation-based approaches [49]. Image pixels are grouped in clusters according to the histogram quantization of images principal components. A Gaussian mixture model is supposed in each cluster. Mahalanobis distance is, then, applied between pixel under test and the center of each cluster. The pixels surpassing the threshold are determined as anomaly pixels. Locally Linear Embedding anomaly detector (LLEAD) is proposed by Kim and Finkel in which the pixels in the images are grouped by k-means clustering method [50]. Therefore, the dimensionality is reduced, and the anomalies are detected.

2.2.3 Matrix Decomposition Based Anomaly Detection

The low rank and sparse matrix decomposition-based methods are introduced as an alternative to RX like methods. They aim to cope with the issues arisen from these traditional anomaly detection methods. According to LRaSMD based approach, the data is decomposed into low rank and sparse parts by using different algorithms. This process can be shown as in the Figure 2.3 below where the original data is presented by the summation of background and anomalies.

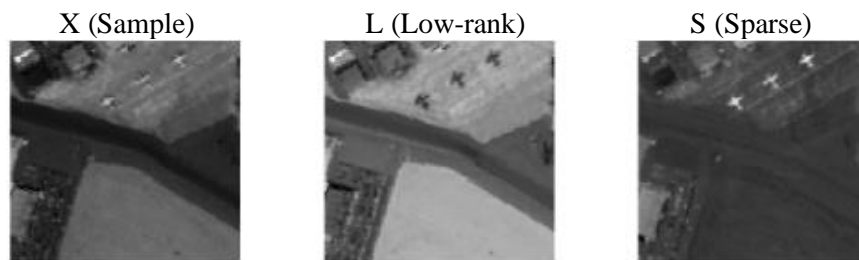


Figure 2.3 X is the observed data, L is the background, and S is the anomalies.

With the obtained parts, the anomaly detectors are built to find anomalous pixels. Different methods use different parts for constructing the anomaly detectors. While some uses low-rank part the others use sparse part of the data.

LRaSMD method is introduced by Sun et al in which the data is decomposed as background and anomaly matrices. They applied GoDec algorithm [51, 52]. Euclidian distance is, then, applied to the sparse part of the data. It is also known as Euclidian distance based LRSMD method. Later, Zhang et al. proposed LRSMD based Mahalanobis Distance (LSMAD) method for hyperspectral anomaly detection [40]. They also use GoDec algorithm in order to get the low-rank and the sparse matrices. After obtaining the background and the sparse matrices, they applied Mahalanobis distance on low-rank part. They claim that their method indicates better detection performance results over the traditional hyperspectral anomaly detection methods. Moreover, an LRSMD based anomaly detector is introduced in [53] in which semisoft GoDec is applied for decomposition. Then, LRX is applied for anomaly detection. Aforementioned methods adopt GoDec algorithm claiming that the results have better performances than using the bilateral random projections (BRP) [54].

However, Yang et al. are proposed an OSP based matrix decomposition anomaly detector in [55] where they claimed that BRP is accelerate the computation. They applied OSP to project the sparse component into the low-rank orthogonal subspace to highlight the anomalies. Another novel anomaly detection method based on Low-Rank and Sparse representation is offered by Xu et al. in [56] in which hyperspectral data is divided as the background and the anomaly matrices. Each pixel in the background is presented by the dictionary and modelled by the low-rank representation. It is claimed that their method has encouraging detection performance. Apart from previously mentioned methods, graph and total variation regularized low-rank representation (GTVLRR) method is proposed in [57]. They claimed that the original LRR model only considers the spectral information of the images. However, the spatial information in HSIs are also important. They take this valuable advantage of the data in addition to spectral signatures. Therefore, total variation (TV) and graph regularization are adopted with LRR. It is claimed that their method achieves the best detection performance. Nevertheless, the computational cost of GTVLRR is high and should be reduced as it is mentioned in the paper.

Sparse representation-based methods express a signal as a linear combination of very few atoms from an overcomplete dictionary consisting of a set of training data from

all the classes. The resulting sparse code can reveal the class information if signals from different classes lie in different subspaces. In the sparsity-based HSI classification model, the spectral signatures of pixels belonging to the same class are assumed to approximately lie in a low-dimensional subspace. In addition to Low-rank and sparse matrix decomposition structure, low-rank part of the data can be represented a linear combination of atoms by adopting sparse representation model. In this thesis, data is decomposed by utilizing matrix decomposition-based algorithm's strategy, and the problem is defined by using sparse representation model or dictionary learning perspective. So, it is distinct from the other methods by modelling the problem. Furthermore, the problem is solved by different approach, and then the anomaly detector is built.

CHAPTER 3

METHODOLOGY

Anomaly detection is an unsupervised hyperspectral target detection technique which aims to separate anomaly pixels from the background, in other words, to detect materials anomalous to their backgrounds. The traditional anomaly detection methods such as RX, and variations of RX generally get information from the background. They subtract the anomalies from the background to distinguish them. However, these methods generally have effective results in homogeneous areas. They can be unreliable when the background is comprised of rare, and large spectral information of anomalies. Because of processing only, the background, and anomaly information may be included in the background in popular anomaly detection algorithms, the LRaSMD based methods [49,52-58] are introduced. They elicit information not only from the background but also from the anomalies. Therefore, an LRaSMD based anomaly detector is proposed in this section by comprising advantage of being unsupervised algorithm of traditional anomaly detection methods, and LRaSMD model.

Current anomaly detection algorithms for comparisons uses GoDec algorithm which estimates low-rank and sparse parts from the data. However, an LADM based decomposition algorithm is applied which also finds the low-rank and sparse structure of the data. Different from previous studies, the decomposition process may be considered a dictionary learning problem where the data is represented as a linear combination of atoms from a dictionary [59]. According to RoSuRe algorithm, atoms in the dictionary are obtained from data samples. By this way, the representative samples can fix and strengthen themselves from errors. Therefore, the data is partitioned, and low-rank and sparse parts are obtained. Mahalanobis distance is, then, applied rather than Euclidean distance. Finally, anomaly detector is built by sparse part different from previous methods, due to holding anomaly information in the sparse component.

3.1 Proposed Method

Hyperspectral image data $X \in \mathbb{R}^{h \times w \times b}$ can be represented as two dimensional data matrix as $X = [X_1, X_2, \dots, X_b]$, $X \in \mathbb{R}^{n \times b}$ where b is the number of spectral bands and $n = h \times w$ is the total number of pixels; in which h is height and w is width. A collection of hyperspectral band vectors $X = \{X_i\}_{i=1}^b \in \mathbb{R}^{n \times b}$ is sampled from union of subspaces $\{S_i\}_{i=1}^k$, where k is the number of subspaces. It then employs the self-representation property of the data to represent each data as a combination of the others [14]. Each band image vector X_i is represented by other band vectors as

$$X_i = XW + S, W_{ii} = 0. \quad (3.1)$$

Equation 3.1 can be transformed into

$$X = XW + S, W_{ii} = 0 \quad (3.2)$$

where block diagonal constraint of W is used for trivial solution that each band is self-represented [14, 60]. With analyses above, the data X is presented by the sum of matrices B and S as $X = B + S$, and $B = BW$ where B is background matrix, S is sparse matrix and W is a diagonal matrix. Thus, the optimization problem can be modeled as in the following equation:

$$\min_{W, S} \|W\|_1 + \lambda \|S\|_1 \text{ s.t. } \begin{cases} X = B + S \\ B = BW \\ \text{diag}(W) = 0, \end{cases} \quad (3.3)$$

where $\lambda > 0$ is a regularization parameter. RoSuRe algorithm [27] is adapted to solve the problem in Eq. (3.3). To efficiently optimize the above problem and to update underlying variables in an alternating fashion, the augmented Lagrangian function [61] is formed as in Eq. 3.4;

$$L(S, W, Y, \mu) = \lambda \|S\|_1 + \|W\|_1 + \langle BW - B, Y \rangle + \frac{\mu}{2} \|(X - S)W - (X - S)\|_F^2. \quad (3.4)$$

By adopting Lagrange function, the problem is simplified and represented in its dual form. Algorithm steps are, then, drawn in between Eqs. 3.5 - 3.9. By using $\hat{W} = I - W$

and minimizing $L(S, W, Y, \mu)$ with respect to W and S with fixed Y ; W and S matrices are updated by using LADM with below equations;

$$W_{t+1} = \arg \min_W \|W\|_1 + \langle B_{t+1}W - B_{t+1}, Y_t \rangle + \frac{\mu}{2} \|BW_{t+1} - B_{t+1}\|_F^2 \quad (3.5)$$

$$S_{t+1} = \arg \min_{W, S} \lambda \|S\|_1 + \langle -B_{t+1}\hat{W}, Y_t \rangle + \frac{\mu}{2} \|B_{t+1}\hat{W}_{t+1}\|_F^2 \quad (3.6)$$

To solve equations Eq. 3.5 and Eq. 3.6 and find W and S matrices $\tau_o(.)$ soft-thresholding operator is used as below:

$$W_{t+1} = \tau_{\frac{1}{\mu Y_1}}(W_t + \frac{B_{t+1}^T((B_{t+1}\hat{W}_t - Y_t)/\mu_t)}{Y_1}), \quad (3.7)$$

$$S_{t+1} = \tau_{\frac{1}{\mu Y_2}}(S_t + \frac{(B_{t+1}\hat{W}_{t+1} - Y_t/\mu_t)\hat{W}_{t+1}^T}{Y_2}) \quad (3.8)$$

where $Y_1 \geq \|L\|_2^2$ and $Y_2 \geq \|\hat{W}\|_2^2$.

Lagrange multipliers Y and μ are updated by

$$Y_{t+1} = Y_t + \mu_t(B_{t+1}W_{t+1} - B_{t+1}), \mu_{t+1} = \rho\mu_t. \quad (3.9)$$

After the algorithm steps are processed, the data is decomposed as low-rank and sparse matrices. The algorithm guarantees that the low-rank part is the closest matrix to the background, and the sparse part is the closest matrix to the anomaly matrix. Nevertheless, the background matrix can contain anomaly pixels. In addition, the anomaly matrix can include non-anomaly information. In order to obtain better statistic maps containing the correct anomaly locations, Mahalanobis distance is applied on the sparse part of the data. By obtained sparse matrix S , Mahalanobis Distance [62, 63] is used to compute the anomaly value for each pixel of S . Anomaly detector is, then, developed as in Eq. 3.10;

$$D(S) = (S - \mu_S)^T \Gamma^{-1} (S - \mu_S) \quad (3.10)$$

where μ and Γ are mean and covariance matrices of S . In addition, the covariance matrix is obtained by the eigen decomposition unlike traditional [64]. The covariance matrix is, then, calculated as in Eq. (3.11);

$$\Gamma = \lambda W^T \quad (3.11)$$

where V and λ represent eigen vectors and eigen values of covariance matrix, respectively. Mahalanobis distance-based anomaly detection methods distinguish anomalies from their background by calculating mean and covariance matrices. The background matrix is computed without eliminating anomalies from the original data in RX and SSRX. As for the LSMAD, the low-rank background matrix is used for building the anomaly detector with Mahalanobis distance. In contrast with LSMAD, Euclidean distance is used in LRaSMD [65]. The distance is applied to the sparse part of the data. As for the proposed method, the problem is defined by dictionary learning point of view. It is solved with an LADM based algorithm by building Lagrange function of the optimization problem. After the decomposition, Mahalanobis distance is applied to the sparse part of the data. It guarantees that the sparse component-based anomaly detector's result is the closest result to the ground-truth matrix of the original data.

3.2 Selected Methods

In this section, selected the state-of-the-art anomaly detection methods are given used for evaluations.

3.2.1 RX anomaly detector

The RX or Global RX (GRX) algorithm, also known as the Mahalanobis distance calculates the distance between a test pixel x , and the mean of the background vector by modelling the background with a multivariate Gaussian distribution with mean and covariance as given by the Eq. 3.12 below:

$$D_{GRX}(x) = (x - \mu)^T \Gamma^{-1} (x - \mu) \quad (3.12)$$

Then, the calculated distance D of the test pixel is called as an anomaly if the distance is larger than a defined threshold.

3.2.2 SSRX anomaly detector

SSRX assumes that target pixels and background statistics can be expressed in different subspaces. It is computed as below

$$D_{SSRX}(x) = (x - \mu)^T (I - WW^\#) (x - \mu) \quad (3.13)$$

where $WW^\#$ is the projection operator. W is a matrix consisting of eigenvectors corresponding to large eigenvalues of background covariance matrix. $W^\#$ denotes the pseudo-inverse of W which is computed by $W^\# = (W^T W)^{-1} W^T$.

3.2.3 LRaSMD anomaly detector

LRaSMD based anomaly detector is mentioned in this section. Firstly, background and anomalies are modelled. Then, the recovery method of the background and anomaly matrices are defined. Finally, the approach of detecting anomalies with the sparse matrix is explained.

The data matrix X is represented by summation of the background B and anomaly matrices S as in Eq. 3.14

$$X = B + S. \quad (3.14)$$

To obtain these matrices, GoDec algorithm which is defined below is applied.

GoDec algorithm

Inputs: $X \in \mathbb{R}^{N \times B}$, the HSI data matrix in 2D form

r , the maximum rank of the background matrix

k , the cardinality of the sparse matrix

ϵ , the error tolerance

Iter, the maximum iteration number

Outputs: B , the low-rank matrix approximation

S , the sparse matrix approximation

Step 1: Initialize: $B_0 = X, S_0 := 0, t := 0, A_1 = \text{randn}(B, r)$

Step 2: Repeat Iter times

- a) $t = t + 1$
 - b) $Y_1 = (X - S_{t-1}) A_1, A_2 = Y_1, Y_2 = (X - S_{t-1})^T A_2$
 - c) If $\text{rank } A_2^T Y_1 < r$ then $r := \text{rank}(A_2^T Y_1)$.
Go to step b); end;
 - d) $B_t = Y_1 (A_2^T Y_1)^{-1} Y_2^T$
 - e) $S_t = P_\Omega(X - B_{t-1})$
- Until $\|X - B_t - S_t\|_F^2 / \|X\|_F^2 < \varepsilon$.

The last part of this method is building the anomaly detector. For this purpose, Euclidian distance is applied on the sparse part of the data as in followed Eq. 3.15

$$D = \sqrt{(S_i - \mu_S)(S_i - \mu_S)^T} \quad (3.15)$$

where μ_S is the mean of the sparse matrix. A larger anomaly value indicates that the pixel belongs to an anomaly with higher probability. Pixels in the image with an anomaly value above a manually selected threshold η are determined to be anomalies.

3.2.4 LSMAD anomaly detector

In this section, another LRSMD method is given. There are two different steps from previous method. First one is using Mahalanobis distance instead of Euclidian distance. The other one is the used matrix when the building the anomaly detector which is the background matrix. It also applies GoDec algorithm for the decomposition. Therefore, anomaly detector is as in below

$$D = (B - \mu) \Gamma^{-1} (B - \mu)^T \quad (3.16)$$

where the mean matrix of the background μ is

$$\mu = \frac{1}{n} (B_1 + \dots + B_n) \quad (3.17)$$

the covariance matrix Γ is

$$\Gamma = \frac{1}{n} (B - \mu)^T (B - \mu) \quad (3.18)$$

$B = [B_1, \dots, B_n]$ is recovered background component and n is the spectral band number.

Due to the given better results, the covariance matrix is computed by different way, which is based on eigen value decomposition [66]. According to eigen decomposition, the covariance matrix is represented in Eq. 3.19,

$$\Gamma = E \Sigma E^T \quad (3.19)$$

Where $E = [E_1, \dots, E_n]$ is the eigen vectors, $\Sigma = \text{diag}(\lambda_1, \dots, \lambda_n)$ is the eigen values and $\lambda_i \geq \lambda_{i+1}$. Mahalanobis distance based anomaly detection methods distinguish anomalies from the background by calculating the mean and covariance matrices. The background matrix is computed without keeping out or separating anomalies from the original data in RX, and SSRX. As for LSMAD, the covariance matrix is obtained with different way of calculation which is eigen decomposition. In LSMAD, data matrix is decomposed into two parts as low-rank and sparse matrices. The sparse matrix consists of non-zero elements, but it can still have background pixels in it.

CHAPTER 4

HYPERSPECTRAL DATASETS

In this chapter, the detailed information about the datasets is given. Hyperspectral image data sets are used to evaluate the effectiveness of the proposed method by comparing with the other selected well-known methods. These data sets having different background and targets are collected with different hyperspectral sensors.

4.1 San Diego Airport

The first data set is San Diego Airport (SDA) in the USA in Figure 4.1, acquired by Airborne Visible/Infrared Imaging Spectrometer (AVIRIS) [67]. The original data has 400×400 pixels and 189 spectral channels in wavelengths from 370 to 2510 nm. The original image data contains the following materials: roof, shadow, grass, and plane. After selecting the area of interest, the subset images in Figures 4.2, 4.3 and 4.4 are obtained.



Figure 4.1 SDA RGB image.

The first subset image has a size of $120 \times 120 \times 189$. It is used for experiments, as illustrated in Figure 4.2. The target objects are indicated in Figure 4.2 (b). There are three planes in the selected image with 58 pixels in total.

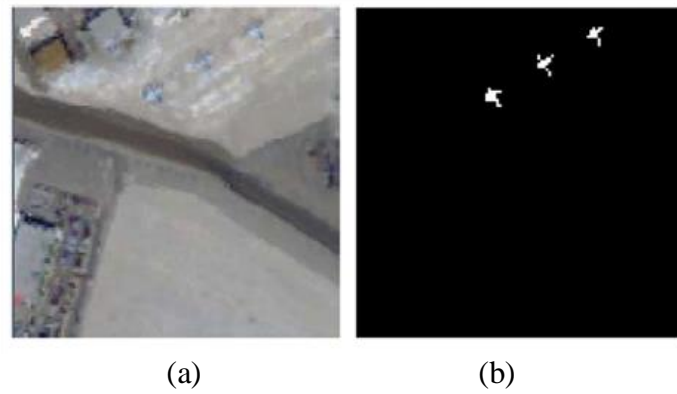


Figure 4.2 SDA (a) subset1 band image. (b) ground truth.

Second subset includes thirteen planes as target. 80×80 area with 189 spectral bands area is selected as seen from the Figure 4.3 (a). There are 226 pixels in total.

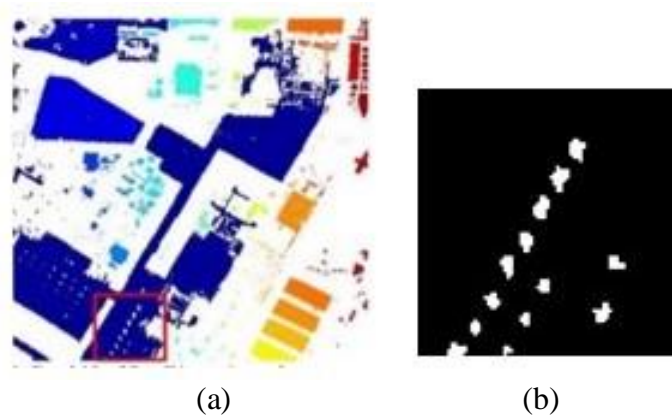


Figure 4.3 SDA (a) subset2 band image. (b) ground truth [68].

The last data obtained from SDA is shown in Figure 4.4. There are two planes to detect.

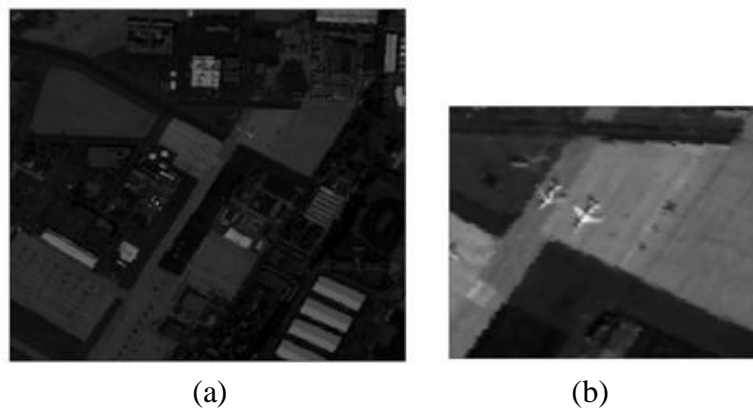


Figure 4.4 SDA (a) subset3 band image. (b) subset1 band image.

4.2 Cri Hyperspectral Data

The second data set in Figure 4.4 has 400×400 pixels with 46 spectral bands in wavelengths from 650 to 1100 nm. It is collected by the Nuance Cri hyperspectral sensor [39]. The data has the materials rock and grass. The target objects are shown in Figure 4.5 (b). There are ten rocks on the grass with 2216 pixels in total.

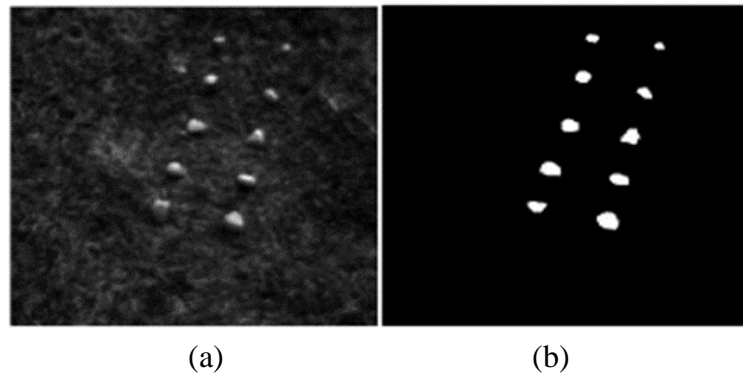


Figure 4.5 Cri image. (a) band image. (b) ground truth.

4.3 Pavia Centre

The third image data is Pavia center in Italy. The original data set has 1096×715 pixels and 102 spectral bands in wavelengths from 430 to 860 nm. It is gathered by the Reflective Optics System Imaging Spectrometer sensor (ROSIS) [69].



Figure 4.6 PaviaC RGB image [70].

The subset sized with $108 \times 120 \times 102$ of the original data set is used for evaluations, as shown in Figure 4.6. The selected area has a bridge, water, and vehicles. There are seven vehicles on the bridge with 43 pixels as shown in Figure 4.6 (b). The bridge and the water are the background materials.

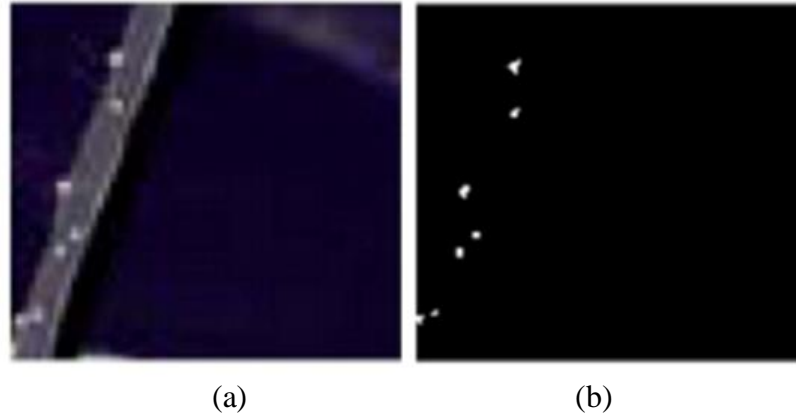


Figure 4.7 PaviaC subset. (a) band image. (b) ground truth.

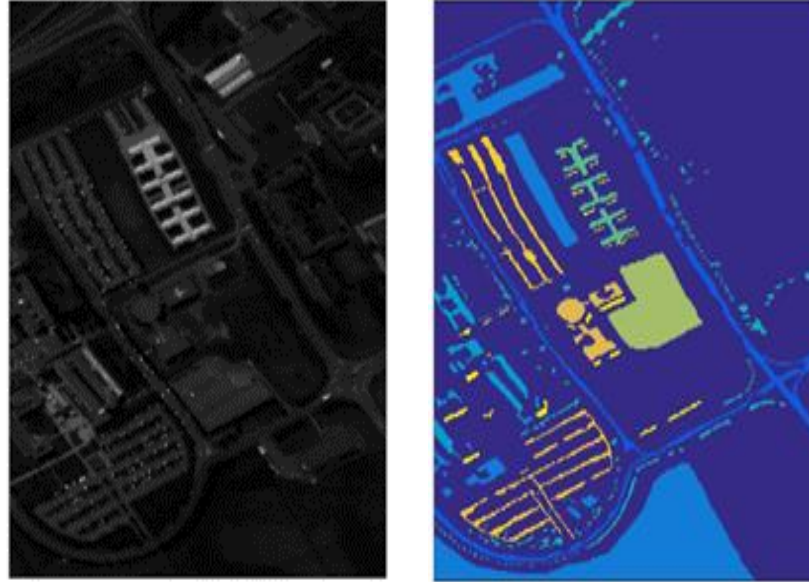
4.4 Pavia University

The dataset is obtained by the ROSIS sensor during a flight campaign over Pavia, northern Italy [71]. The number of spectral bands is 103 for Pavia University (PaviaU). The original image size is 610×340 pixels. The geometric resolution is 1.3 meters.



Figure 4.8 PaviaU RGB image.

PaviaU dataset is acquired from the ROSIS sensor during a flight over Pavia University, northern Italy. The dataset is shown in Figure 4.9. The image ground truth differentiates 9 classes. Figure 4.9 represents band image, ground truth classes, and the fields in the data.



(a)

(b)

Groundtruth classes for the Pavia University scene and their respective samples number

#	Class	Samples
1	Asphalt	6631
2	Meadows	18649
3	Gravel	2099
4	Trees	3064
5	Painted metal sheets	1345
6	Bare Soil	5029
7	Bitumen	1330
8	Self-Blocking Bricks	3682
9	Shadows	947

(c)

Figure 4.9 PaviaU. (a) band image. (b) ground truth classes. (c) classes with fields [72].

In all images after this section, we pick up a sample from the datasets ground truth classes. As mentioned previously, we created new datasets and their ground truths according to chosen samples from PaviaU ground truth classes. At last, we call these samples as targets in each image.

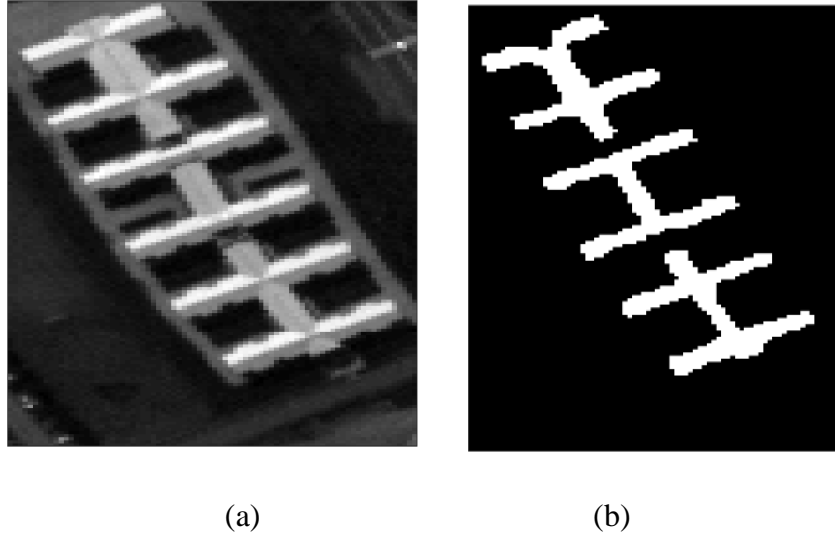
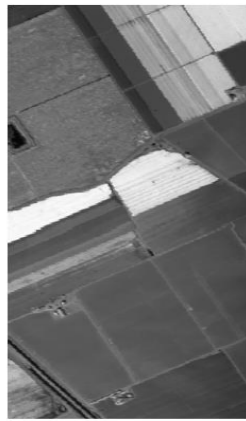


Figure 4.10 PaviaU. (a) Sample 5 band image. (b) ground truth.

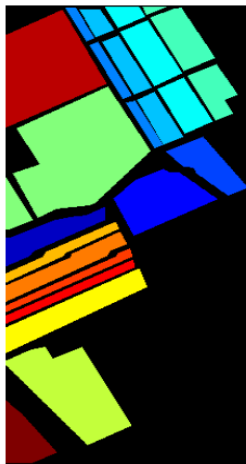
The images shown in Figure 4.10 is constructed by choosing sample 5 which is painted metal sheets with 1345 pixels. We cropped the area sized with $140 \times 80 \times 103$ which includes the all anomaly pixels belongs to this sample. It contains the materials 1, 2, 4, 5, 6, 8, and 9.

4.5 Salinas

The fourth dataset is Salinas hyperspectral image shown in Figure 4.11. It is acquired by the AVIRIS sensor over Salinas Valley, California. It is characterized by high spatial resolution 3.7-meter pixels. The image data is sized with 512×217 pixels with 224 spectral band numbers. The 20 water absorption bands which are 108-112, 154-167, and 224, are eliminated. This image is available only as at sensor radiance data. The dataset contains the materials of vegetables, bare soils, and vineyard fields. Its ground truth contains sixteen classes.



(a)



(b)

Groundtruth classes for the Salinas scene and their respective samples number

#	Class	Samples
1	Brocoli_green_weeds_1	2009
2	Brocoli_green_weeds_2	3726
3	Fallow	1976
4	Fallow_rough_plow	1394
5	Fallow_smooth	2678
6	Stubble	3959
7	Celery	3579
8	Grapes_untrained	11271
9	Soil_vinyard_develop	6203
10	Corn_senesced_green_weeds	3278
11	Lettuce_romaine_4wk	1068
12	Lettuce_romaine_5wk	1927
13	Lettuce_romaine_6wk	916
14	Lettuce_romaine_7wk	1070
15	Vinyard_untrained	7268
16	Vinyard_vertical_trellis	1807

(c)

Figure 4.11 Salinas. (a) band image. (b) ground truth classes. (c) classes with fields [73].

In this section, three datasets are obtained from the original data. One is acquired by cropping Salinas dataset sized with $200 \times 150 \times 204$ as shown in Figure 4.12. The anomaly pixel number is 42. The other one is the synthetic data where anomalies are implemented. There are 185 anomaly pixels in total.

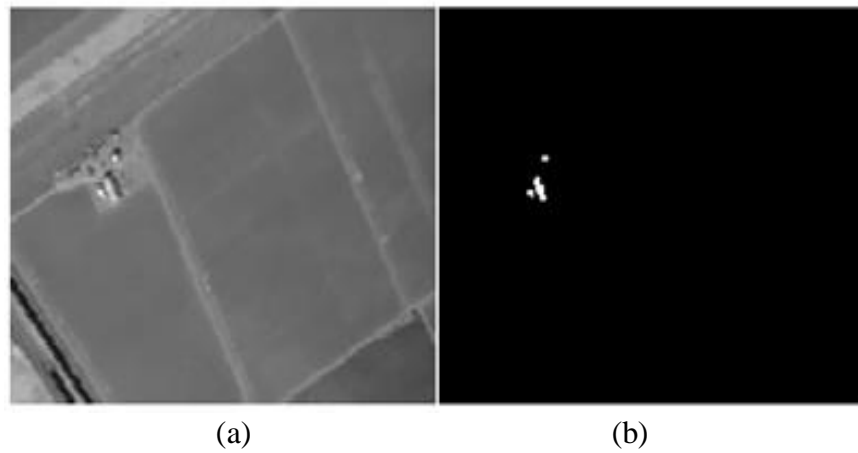


Figure 4.12 Salinas Real. (a) band image. (b) ground truth [74].

To obtain a synthetic anomaly, the target implant method is used [50]. The 150×126 binary mask image M shown in Figure 4.13 (b) has been constructed by generating six squares having sides measuring from 1 to 6 pixels arranged in a line. The six squares have been then copied in reverse order and arranged in another line at close distance. The two lines have finally been rotated by an angle of approximately $\pi/6$. The pixels inside the squares have value of 1, while the rest of the pixels in M have value 0. Then, a region I is cropped from the scene, having the same dimension as the mask, and we built the modified image I' containing the implanted targets, given a parameter k with the values 4 and 14 [75]. Therefore, two datasets are obtained by aforementioned information: Implemented4 126×150 and Implemented14 150×200 in Figure 4.13.

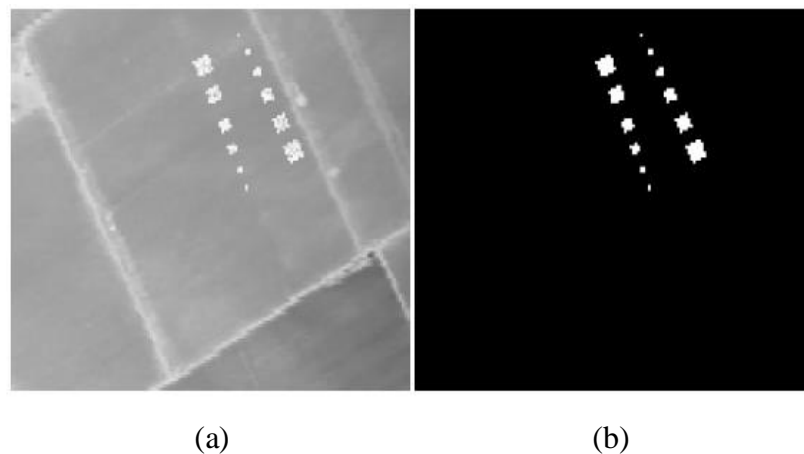
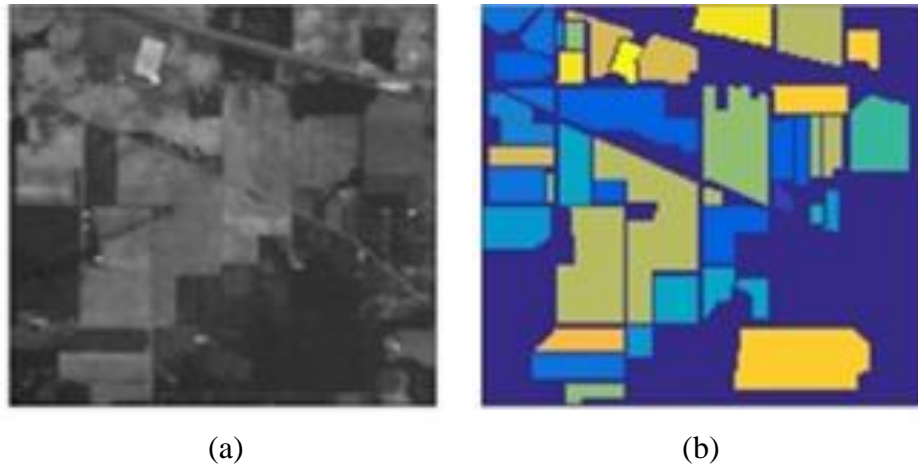


Figure 4.13 Salinas synthetic data. (a) band image. (b) ground truth [74].

4.6 Indian Pines

The dataset is acquired by AVIRIS sensor over the Indian Pines test site in North-western Indiana. It consists of 145×145 pixels and 224 spectral reflectance bands in the wavelength range $0.4\text{--}2.5 \times 10^{-6}$ meters as shown in Figure 4.14. The Indian Pines scene contains two-thirds agriculture, and one-third forest or other natural perennial vegetation. There are two major dual lane highways, a rail line, as well as some low-density housing, other built structures, and smaller roads. Since the data is obtained in June some of the crops present, corn, soybeans, are in early stages of growth with less



Groundtruth classes for the Indian Pines scene and their respective samples number

#	Class	Samples
1	Alfalfa	46
2	Corn-notill	1428
3	Corn-mintill	830
4	Corn	237
5	Grass-pasture	483
6	Grass-trees	730
7	Grass-pasture-mowed	28
8	Hay-windrowed	478
9	Oats	20
10	Soybean-notill	972
11	Soybean-mintill	2455
12	Soybean-clean	593
13	Wheat	205
14	Woods	1265
15	Buildings-Grass-Trees-Drives	386
16	Stone-Steel-Towers	93

(c)

Figure 4.14 Indian Pines. (a) band image. (b) ground truth classes. (c) classes with fields [76].

than 5% coverage. The ground truth available is designated into sixteen classes and is not all mutually exclusive. The number of bands are reduced to 200 by removing bands of 104-108, 150-163, and 220 which covers the region of water absorption. Indian Pines data is available on University of Pursuer's Multi-speed site.

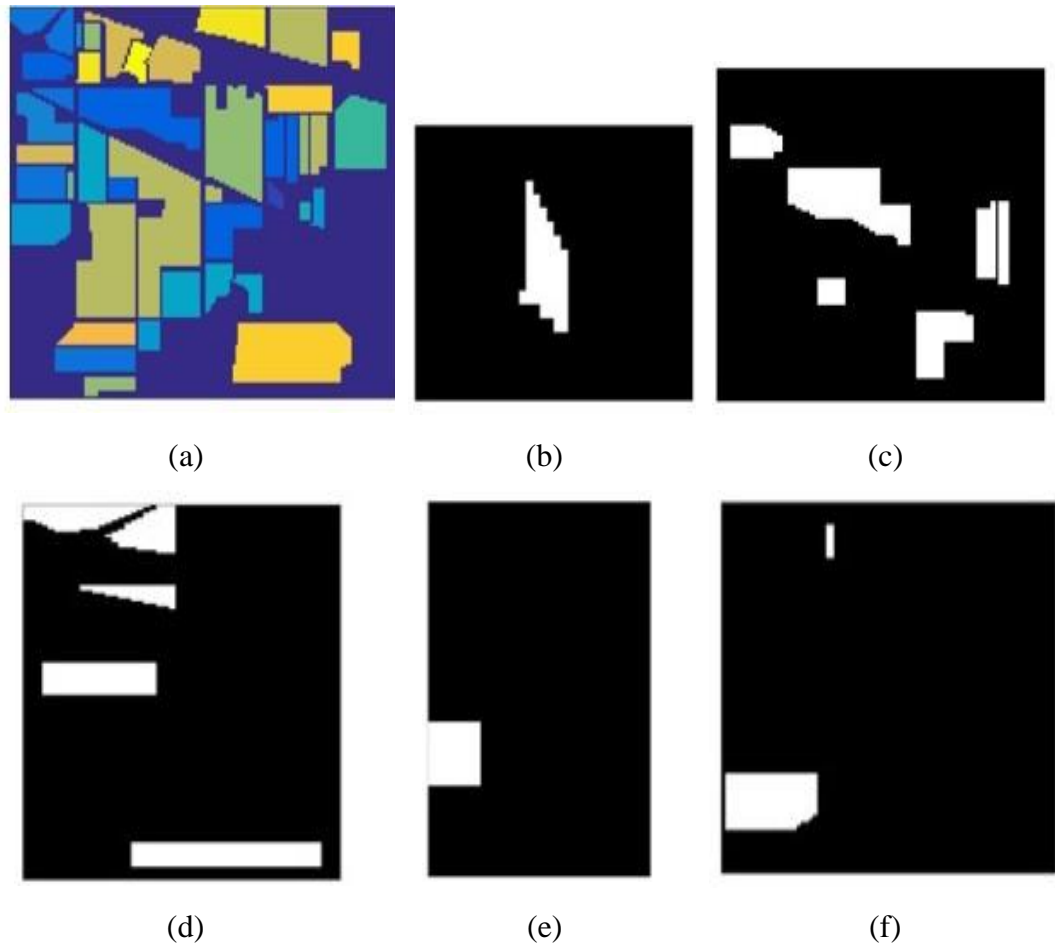


Figure 4.15 Indian Pines. (a) Classes. (b) Sample 1. (c) Sample 2. (d) Sample 3. (e) Sample 4. (f) Sample 5.

Figure 4.15 shows Indian pines classes with the selected area for the sample 1, 2, 3, 4, and 5, and their respected ground truths. The subsets are acquired by selecting each sample as anomaly target. The maps contain the materials alfalfa, corn-notil, corn-mintill, corn, and grass-pasture, respectively. Figure 4.15 b) is for sample 1 sized with 20×40 pixels and 46 anomaly pixels, c) is for sample 2 sized with 100×120 and 1428 anomaly pixels. The next data is selected as 140×50 for sample 3. There are 830

anomaly pixels. Figure 4.15 e) is for sample 4 which is cropped as 40×20 with 35 anomaly pixels. The last one is grass pasture that is sample 5. It has 336 anomaly pixels.

4.7 Airport Beach Urban Data

Airport–Beach–Urban (ABU) Data Set: Figures 4.16-4.21 present the images and their ground truths in the ABU data set. The subset images are sized with 100×100 . The ground truths are labeled with the Environment for Visualizing Images (ENVI) software [77]. In addition, the spatial resolutions of the images are also different due to the different heights of the flights. The ABU data set has been made available on the first author's homepage [78].

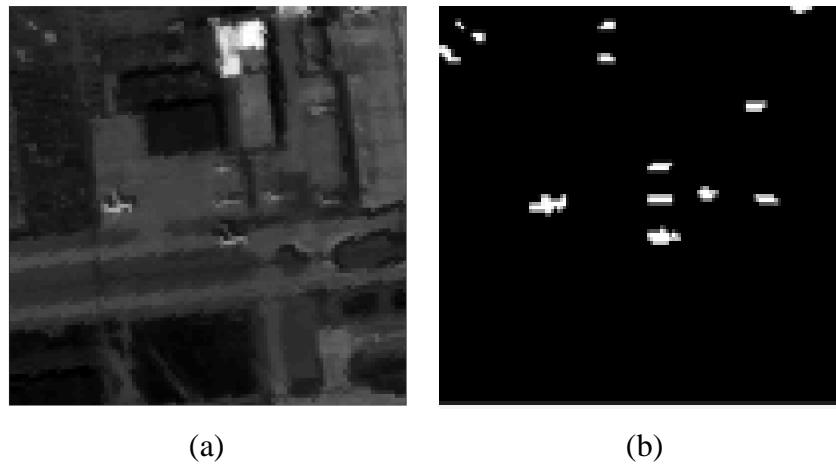


Figure 4.16 ABU airport 1. (a) band image. (b) ground truth.

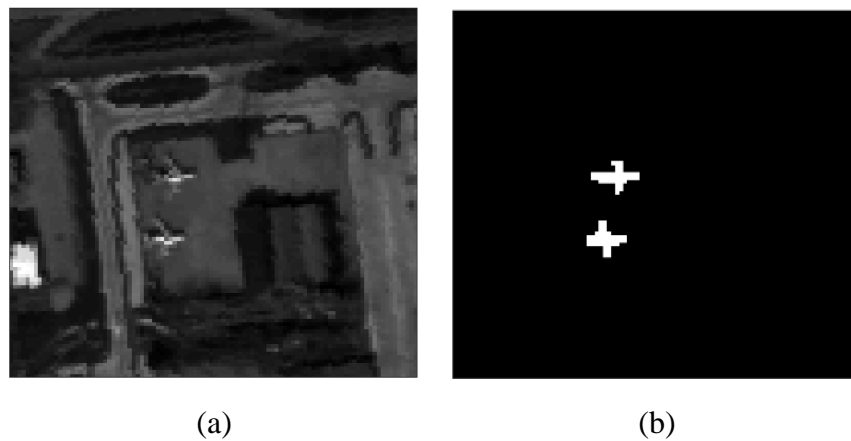


Figure 4.17 ABU airport 2. (a) band image. (b) ground truth.

Figure 4.16 demonstrates ABU airport 1 data details with a single band image and its reference map, respectively. It is captured by AVIRIS sensor in Los Angeles with 7,1m resolution. The target objects are planes with 144 pixels in total. Figure 4.17 is for airport 2 data which is captured by AVIRIS sensor in Los Angeles with 7,1m resolution. There are two planes as target. The total number of pixels for target of interest is 87.

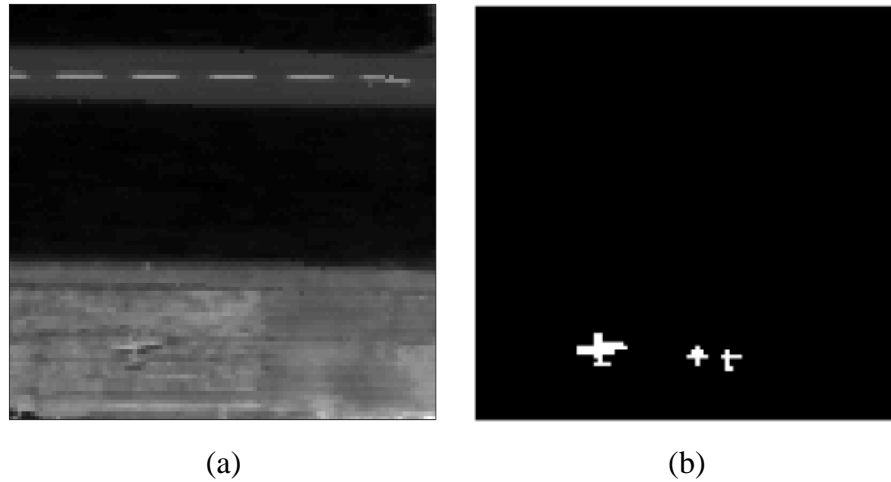


Figure 4.18 ABU airport 4. (a) band image. (b) ground truth.

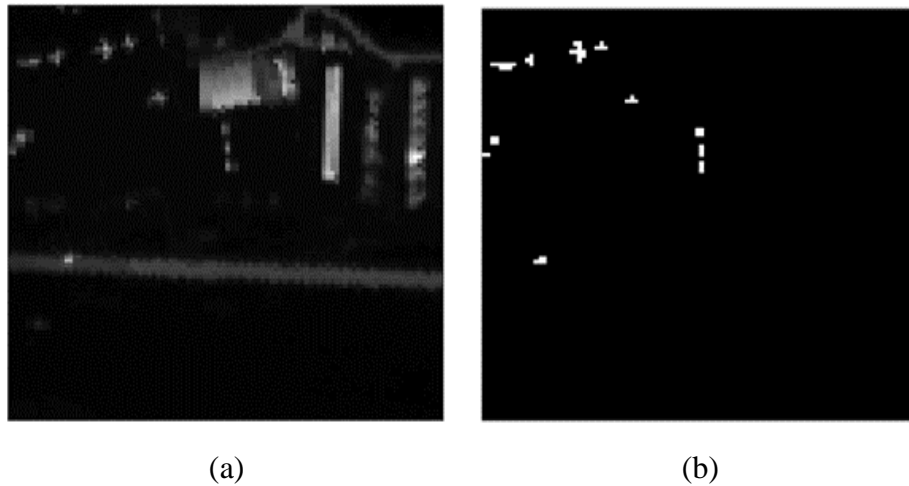


Figure 4.19 ABU urban 3. (a) band image. (b) ground truth.

Figure 4.18 is airport 4 which is captured by AVIRIS sensor in Gulfport with 3.4m resolution. There are three planes as object of interest with 60 pixels, in total. Figure 4.19 is for urban 3 data which is captured by AVIRIS sensor in Gainesville with 3.5 m resolution. Total number of anomaly pixels is 272. Figure 4.20 shows urban 4 image and its ground truth. It has resolution 7.1m captured by AVIRIS sensor in Los Angeles.

The total number of anomaly pixels is 272. Figure 4.21 is for urban 5 data which is captured by AVIRIS sensor in Gainesville with 3.5 m resolution. Total number of anomaly pixels is two hundred seventy-two. Figure 4.20 shows urban 4 image and its ground truth. It has resolution 7.1m captured by AVIRIS sensor in Los Angeles. The total number of anomaly pixels is 232.

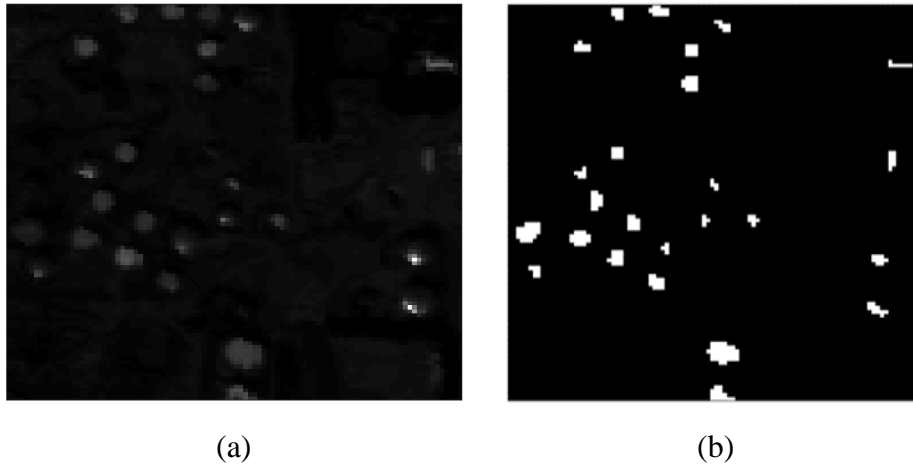


Figure 4.20 ABU urban 4. (a) band image. (b) ground truth.

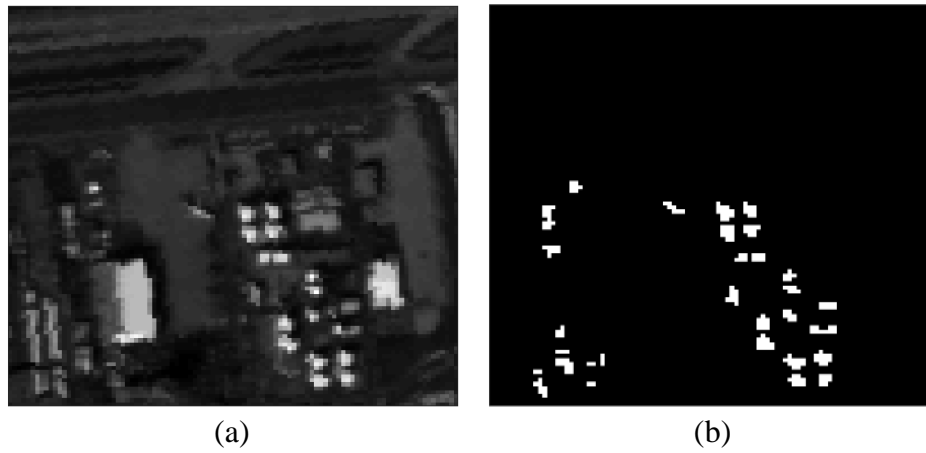


Figure 4.21 ABU urban 5. (a) band image. (b) ground truth.

CHAPTER 5

EXPERIMENTAL RESULTS

5.1 Experimental Setup

In this section, information about the parameters is given. The parameters rank value r and cardinality value k are involved in LSMAD and LRaSMD. For GRX, no parameter is involved in the detector during experiments setting. For SSRX, the number of eigen vectors corresponding to large eigen values, which are close to background classes, are selected for each image data. The rank value r is set to 1 for PaviaC image and 2 for Cri and SDA images for the LSMAD as claimed the best results obtained with these parameters. In the LRaSMD method, r is set to 1 for PaviaC as it is in the study. The rank value r is set to 2 for Cri and SDA images as mentioned in the LSMAD study. The cardinality parameter k is set to the proportions of the anomalies in each image. Thus, the initial value for the parameters r and k values for the LSMAD and LRaSMD methods are set as they are mentioned as the best values in the literature. The rank value r is set for 1 for Salinas and Indian pines and is set for 2 for ABU airport and urban images in LRaSMD and LSMAD methods.

5.2 Experimental Results

In this part, two dimensional results of compared anomaly detectors are given for each dataset. Figure 5.1 shows all two-dimensional results for the methods SLRMD, LSMAD, LRaSMD, SSRX, and GRX from left to right, respectively.

For the first dataset, plane locations are clearly seen in SLRMD and LRaSMD. However, LRaSMD finds the other pixels such roofs which means it has more false alarms. As for second dataset, four methods have similar results showing planes except from GRX, which does not show anomaly locations. Two planes in SDA subset 3 are clear than the other methods in proposed method. LRaSMD and SSRX have similar results which is close to GRX, but GRX has more false alarms. LSMAD has the highest false alarms and do not show anomalies better. Overall, the planes in the first three

datasets as an anomaly are detected visually better than the other methods by the proposed method. As for Cri datasets in Figure 5.1 d), nearly all rocks can easily be selected from the results except from GRX. Nevertheless, rocks in the proposed result image is clearer than the other.

The next data includes seven vehicles which are detected for the first three methods visually better than the last two ones. When AUC values are considered proposed method finds anomaly pixels with highest performance. Up to now, the datasets are used for the paper gives visually better two-dimensional results, which are SDA subset 1, Cri, and PaviaC in Figure 5.1 a), d) and e), respectively. The next dataset is PaviaU subset for sample 5, painted metal sheets. The result for the proposed method in the first column has the most similar results to ground truth which shows all anomaly locations better than the others. However, the others do not show a great deal of anomaly pixels compared with their anomaly map. For Salinas real dataset, proposed method has found the anomaly locations visually better than the others. LRaSMD seems to present anomaly locations better but it detects other materials as well. LSMAD and SSRX and GRX seem to have similar results. GRX has less false alarm between them. The next two results are for the Salinas implemented data. Proposed method illustrates anomaly pixels better than the others. It finds anomaly locations the best in the imp 14 data. For imp-4 data SLRMD and SSRX seem to have similar results. Nevertheless, anomaly locations are clearer in the SLRMD. As for imp-14 SLRMD shows similar results with LRaSMD. When AUC values are compared proposed method has superiority both visually and numerically over the others. In general, all methods performances get higher in the imp-14 data than the imp-4. The result for the Indian pines between Figures 5.1 j)-n) do not visually show anomaly locations well. It can be claimed that they are not suitable to discriminate for vegetables. They may not be appropriate for the datasets only containing similar structure of agricultural materials. However, proposed method shows anomaly pixels better for samples 1, 4, and 5, which are distinct from the others, and have AUC values higher than 84%. The last six dataset's target materials are the planes. SLRMD has visually better results than the other ones for ABU airport 1 data. The other methods have similar scenes except from GRX. For the next one, the anomalies can be selected. They are shown in

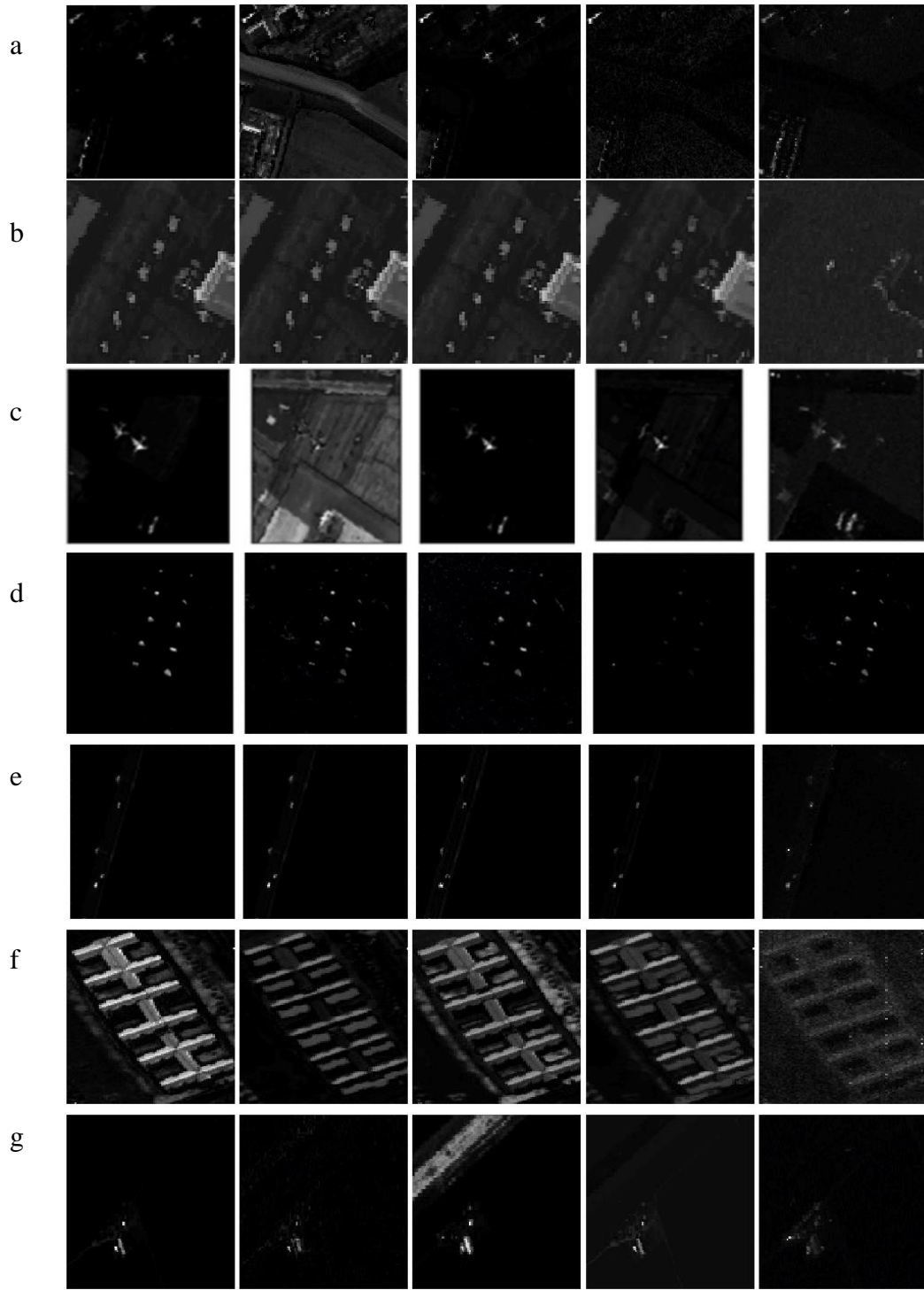


Figure 5.1 Two-dimensional results for the a) SDA subset 1. b) SDA subset 2. c) SDA subset 3. d) Cri. e) PaviaC. f) PaviaU sample 5. g) Salinas real. h) Salinas imp4. i) Salinas imp14. j) Indian Pines sample 1. k) Indian Pines sample 2. l) Indian Pines sample 3. m) Indian Pines sample 4. n) Indian Pines sample 5. o) ABU airport 1. p) ABU airport 2. q) ABU airport 4. r) ABU urban 3. s) ABU urban 4. t) ABU urban 5. (a) SLRMD. (b) LSMAD. (c) LRaSMD. (d) SSRX. (e) GRX.

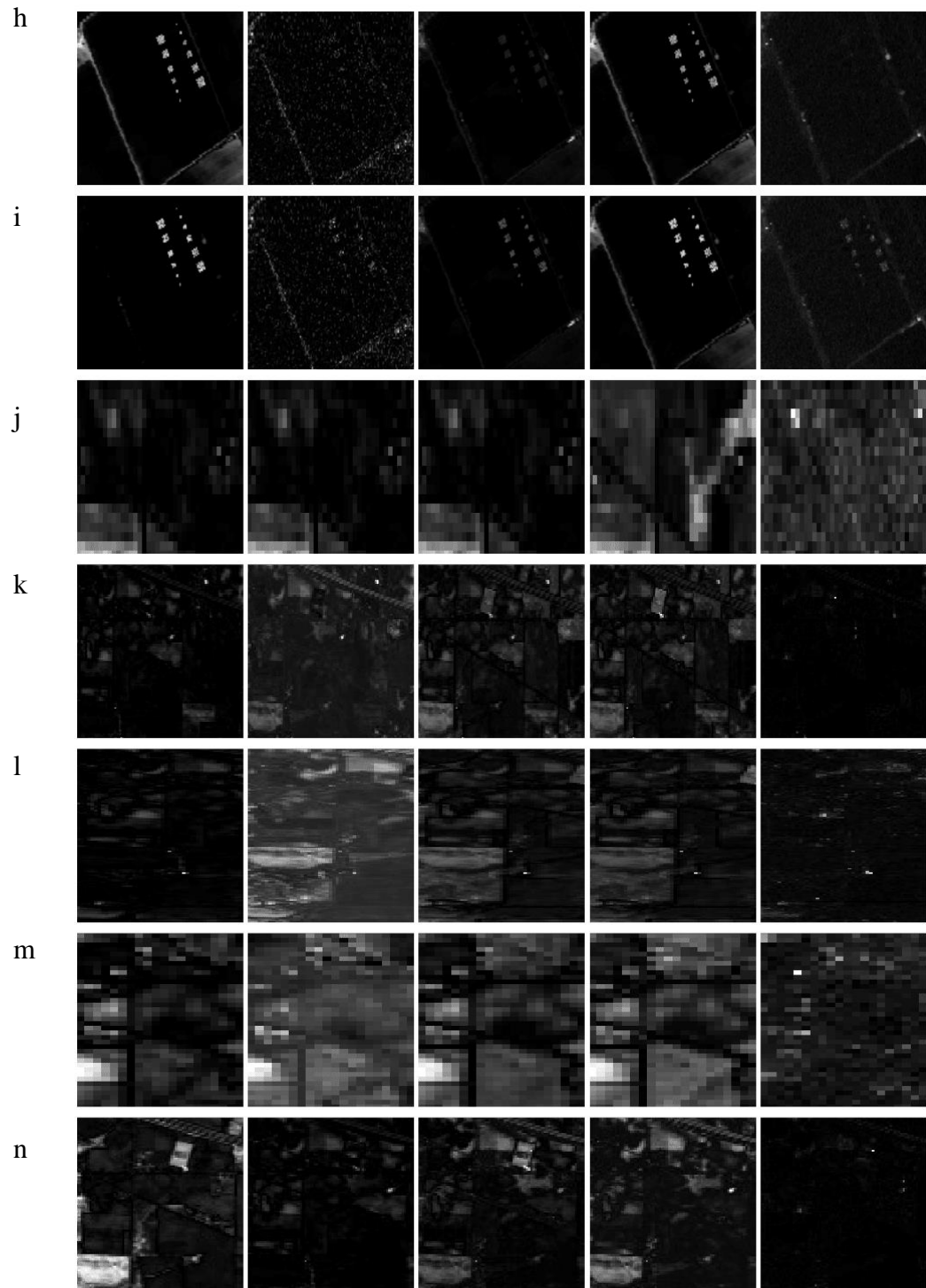


Figure 5.1 (continue) Two-dimensional results for the a) SDA subset 1. b) SDA subset 2. c) SDA subset3. d) Cri. e) PaviaC. f) PaviaU sample 5. g) Salinas real. h) Salinas imp4. i) Salinas imp14. j) Indian Pines sample 1. k) Indian Pines sample 2. l) Indian Pines sample 3. m) Indian Pines sample 4. n) Indian Pines sample 5. o) ABU airport 1. p) ABU airport 2. q) ABU airport 4. r) ABU urban 3. s) ABU urban 4. t) ABU urban 5. (a) SLRMD. (b) LSMAD. (c) LRSMD. (d) SSRX. (e) GRX.

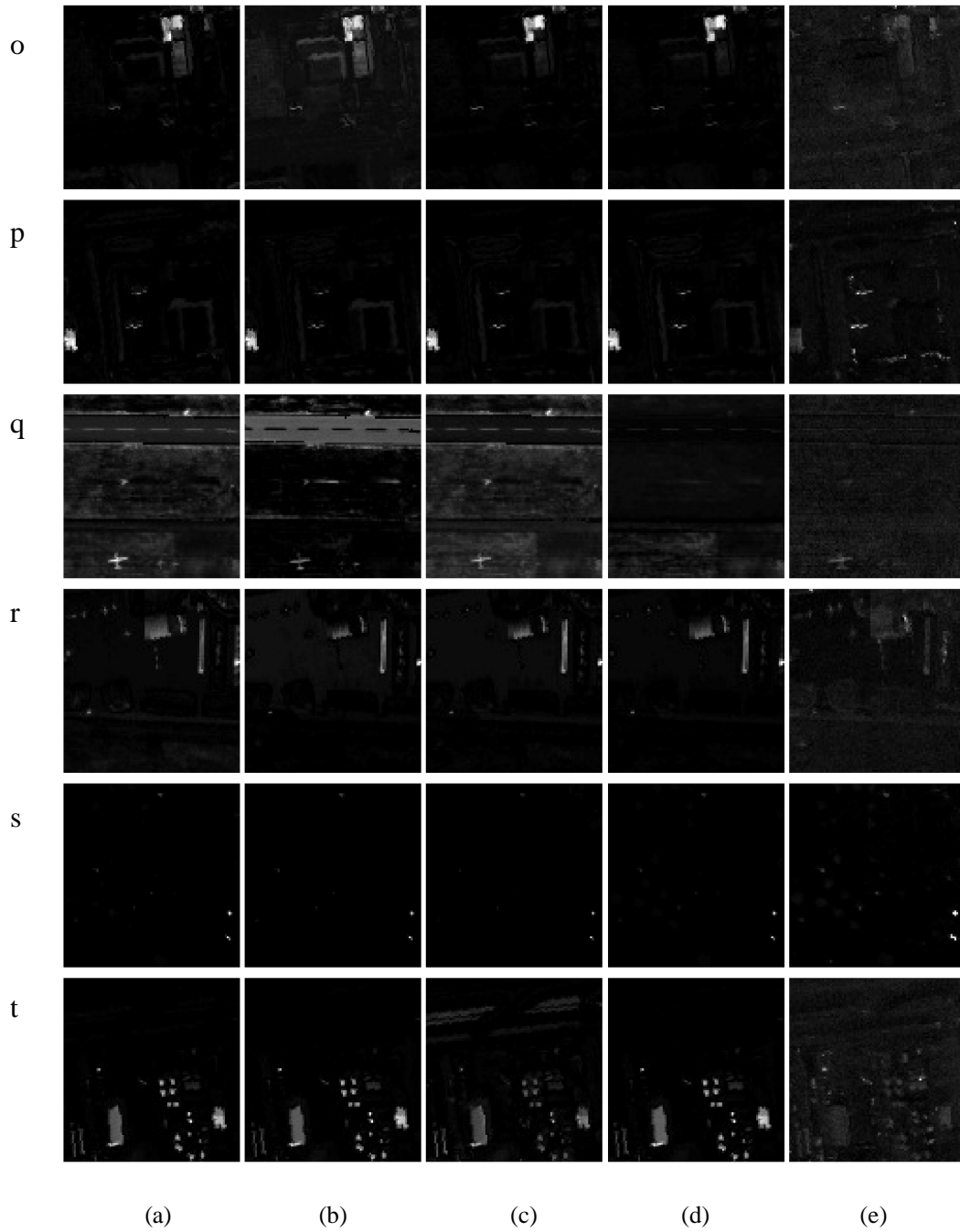


Figure 5.1 Two-dimensional results for the a) SDA subset 1. b) SDA subset 2. c) SDA subset3. d) Cri. e) PaviaC. f) PaviaU sample 5. g) Salinas real. h) Salinas imp4. i) Salinas imp14. j) Indian Pines sample 1. k) Indian Pines sample 2. l) Indian Pines sample 3. m) Indian Pines sample 4. n) Indian Pines sample 5. o) ABU airport 1. p) ABU airport 2. q) ABU airport 4. r) ABU urban 3. s) ABU urban 4. t) ABU urban 5. (a) SLRMD. (b) LSMAD. (c) LRaSMD. (d) SSRX. (e) GRX.

SLRMD better. For airport 4 data, the plane is easily seen in SLRMD results. It is selectable for the other methods. The results in Figure 5.1 s) and t) do not have clear

vision. One can visually see the planes in the last data for all methods. The methods have similar scenes apart from GRX. Overall, the anomalies are the clearest in Figure 5.1 p), q), and t) for the proposed method.

In addition to the image's results published in the paper, SDA subset 3, Salinas real and implemented images show anomaly locations visually better than the other methods, and the other datasets with the highest AUCs.

5.3 Performance Analysis

In this section, we provide the experimental results to validate the effectiveness of the proposed method. The detection performance of the proposed method is evaluated and compared with the following state-of-the-art anomaly detection techniques: LSMAD, LRSMD, GRX, and SSRX. The detection performances are evaluated by drawing the Receiver Operating Characteristic (ROC) curves and calculating the Area Under the ROC Curve (AUC) values [79,80]. The ROC curve describes detection performance with probability of detection (Pd) or true positive rate (TPR) plotted as a function of probability of false alarm rate (Pfa) or false positive rate (FPR). When applied to the test statistic with known ground truth, these probabilities are estimated by the following equations:

$$TPR = TP/(TP+FN) \quad (5.1)$$

$$FPR = FP/(FP+TN) \quad (5.2)$$

where TP, TN, FP, and FN represent true positive, true negative, false positive, and false negative, respectively. The threshold can be changed across the range of the test statistic to obtain a group of pairs (Pfa, Pd), which can be used to generate the ROC curve.

The other the most widely used metric for anomaly detection evaluation is AUC metric refers to the area under the ROC curve (encircled by the ROC curve and the false alarm rate axis). The AUC value providing a numerical accuracy measure is used to analyze the detection performance quantitatively. When the AUC value is 1, it stands for the

perfect test. Specifically, given a detection map and a reference map, the AUC value is calculated as in Eq. 5.3:

$$AUC = \int_{-\infty}^{\infty} Pfa(t)Pd(t)dt = \int_0^1 Pfa(t)Pd(t)dt \quad (5.3)$$

where Pd defines how many correct positive results occur among all positive samples, when the threshold for the detection map is set as t. Pfa, on the other hand, defines how many incorrect positive results occur among all negative samples available. The advantage of the AUC metric is that it depends only on the order of the pixels rather than absolute detection values. Therefore, AUC is adopted in the study to evaluate the objective performances of different methods. Furthermore, as suggested in [37], ROC curves and confidence intervals are also used in the study for objective evaluation. When dealing with empirical distributions the integral is replaced by a sum [17].

Numerical results are listed in Table 5.1 representing the AUC values of each method which are calculated by the information of Pfa and Pd values in ROC plots, as shown in Figure 5.2. SDA subset 1 data SLRMD has the highest AUC value with 99% followed by LRaSMD with 98%, SSRX about 95%, GRX with 75%, and LSMAD with 58% which is the lowest. As for SDA subset 2, AUC values are close to each other for four methods on average 72% except from GRX which as the lowest with 52%. However, proposed method still has the highest with 73%. Anomaly materials is better founded for CRI dataset about 98% for SLRMD followed by SSRX, GRX, LSMAD, and LRaSMD, respectively. For PaviaC, the AUC values around 99% for all methods apart from LRaSMD with 96%. For PaviaU sample 5, SLRMD explicitly has the highest 96% followed by LRaSMD where LSMAD has the lowest AUC at 73%. Salinas real data has the highest AUC values at 99% for three methods: SLRMD, LRaSMD, GRX where SLRMD has the best one. They are followed by SSRX, and LSMAD. As for Salinas synthetic data, the proposed method has 99% followed by LRaSMD and SSRX. While k value is increased from 4 to 14 during implementation of anomalies, AUC values become higher in imp 14 than imp 4 for all methods. This increase rate is the highest in GRX and LSMAD. So, GRX and LSMAD has better performance result in imp 14 data. The next five datasets are constructed from Indian

Table 5.1 AUC values of the methods for hyperspectral data sets.

AUC	SLRMD	LSMAD	LRaSMD	SSRX	GRX
SDA subset 1	0.9937	0.5820	0.9888	0.9490	0.7530
SDA subset 2	0.7311	0.7232	0.7231	0.7122	0.5237
CRI	0.9773	0.8822	0.7845	0.9637	0.9146
PaviaC	0.9998	0.9997	0.9689	0.9949	0.9982
PaviaU s5	0.9630	0.7357	0.9121	0.8693	0.8492
Salinas Real	0.9992	0.8530	0.9917	0.9754	0.9979
Salinas imp-4	0.9954	0.7214	0.9839	0.9941	0.7463
Salinas imp-14	0.9999	0.8462	0.9934	0.9952	0.9862
Indian Pines s 1	0.8411	0.217	0.2203	0.2288	0.5226
Indian Pines s2	0.6945	0.5987	0.5773	0.5789	0.5226
Indian Pines s3	0.6102	0.5584	0.4593	0.4416	0.4565
Indian Pines s4	0.8379	0.6891	0.7757	0.7322	0.5208
Indian Pines s5	0.9543	0.6382	0.9184	0.9441	0.5232
ABU airport1	0.8124	0.5753	0.6218	0.6127	0.811
ABU airport2	0.8957	0.6657	0.6792	0.7059	0.8418
ABU airport4	0.9429	0.8099	0.8849	0.5856	0.8704
ABU urban3	0.9703	0.4856	0.6983	0.8691	0.8854
ABU urban4	0.994	0.97	0.969	0.991	0.966
ABU urban5	0.9562	0.9403	0.9145	0.9476	0.9523
Overall	0.904	0.71	0.793	0.794	0.771

pinces data. Proposed method has the highest AUC value in sample 5 (grass pasture) with 95% which is followed by sample 1 (alfalfa) and sample 4 (corn) about 84%. The other methods perform the best in sample 5 between the other samples about nineties in LRaSMD and SSRX. Apart from SLRMD, LSMAD, and SSRX, the remaining methods have less AUC values in all other samples. The last datasets are ABU airport and urban datasets. For airport 1 and 2 data, SLRMD detects planes with 81% and

89%. As for other datasets, proposed method has the highest AUC values above 94% till 99% for urban 4 image. In general, GRX results come after proposed method that are the closest results in urban and airport 1 images. The other methods, LSMAD, LRaSMD, and SSRX, have the next higher AUC values for all datasets, in turn. To exemplify, LRaSMD has higher value than SSRX in airport 4. However, it has less value than SSRX in urban 3. Overall results in Table 5.1 considered, it can be stated that the proposed method has higher AUC values of >90% on average, which can be considered as an encouraging performance for detecting anomalies.

In addition to Table 5.1, AUC values are categorized according to different materials. The results are presented in Table 5.2. According to these results, SLRMD detects vehicles about 99% which is the highest value. It is followed by Salinas Real and synthetic datasets which are also about 99%. Then, it can be seen that the proposed

Table 5.2 AUC values for the datasets according to materials.

AUC	SLRMD	LSMAD	LRaSMD	SSRX	GRX
plane	0.8752	0.6712	0.7796	0.7131	0.76
vehicle	0.9998	0.9997	0.9689	0.9949	0.9982
rock	0.9773	0.8822	0.7845	0.9637	0.9146
implemented	0.998	0.7838	0.989	0.995	0.866
vegetables	0.788	0.54	0.59	0.585	0.509
painted metal	0.9630	0.7357	0.9121	0.8693	0.8492
Salinas Real	0.9992	0.8530	0.9917	0.9754	0.9979
ABU urban	0.9735	0.7986	0.8606	0.9359	0.9346

method results are above 79% according to categorized results, which is still the highest. The other methods have values between 50 and 60 percent as the least AUC value, which are close to each other. When all methods are considered, they all detect vehicles with higher values which is 99% except from LRaSMD which is 96%. As for Salinas real data, SLRMD, LRaSMD, and GRX have competitive results. When the results in Table 5.2 and Figure 5.1 are considered vehicles, Salinas real and implemented data, rocks, and planes are detected with higher performance.

Finally, overall AUC values are presented in the last row of Table 5.1. According to this table, SLRMD has the highest AUC values with about 90% which is followed by GRX, SSRX, LRaSMD, and LSMAD, respectively. GRX has the most competitive result with approximately 80%. LSMAD has the lowest AUC values with 71% in overall. Nevertheless, LSMAD has generally the second highest AUC values when the anomaly materials considered separately. However, proposed method has distinct result with nineties percent, in overall. The others have the results with seventies percent.

Figure 5.2 shows the ROC plots for the methods for each dataset. First data is SDA subset 1. The results indicate that SLRMD method outperforms other methods with 0.001 FAR. It reaches 100% Pd with less FAR. It is followed by LRaSMD method with 0.1 FAR when reaching 100% Pd. They are followed by SSRX, GRX, and LSMAD, respectively with more FAR at 100% Pd. As for SDA subset 3, SLRMD, LSMAD, and LRaSMD have similar plot. These three lines are always above SSRX and GRX which means they have higher Pd values with less FAR. As for CRI results in Figure 5.2 c), SLRMD method shows better performance than the other methods which has the highest Pd value between 0.00001 and 0.1 FAR. The ROC curve is always above other methods. According to PaviaC, SLRMD and LSMAD methods are distinct from the other methods and have better performance. Although the results of the proposed method and LSMAD seem to have similar probability of detection values, SLRMD method have slightly better performance than the LSMAD method according to Table 5.1. When SLRMD and LSMAD methods, in addition, have similar FARs between 0.0001 and 0.001, SLRMD has higher Pd values than LSMAD. The next data's result is for PaviaU in Figure 5.2 e). All methods have similar results with 0.001 FAR up to 0.1 Pd apart from GRX. After that point, proposed method is always above the other lines with higher Pd and less FAR. SLRMD detection rate peaks between 0.01 and 0.1 FAR about 99%Pd. The other methods follow each other with closer Pd and FAR.

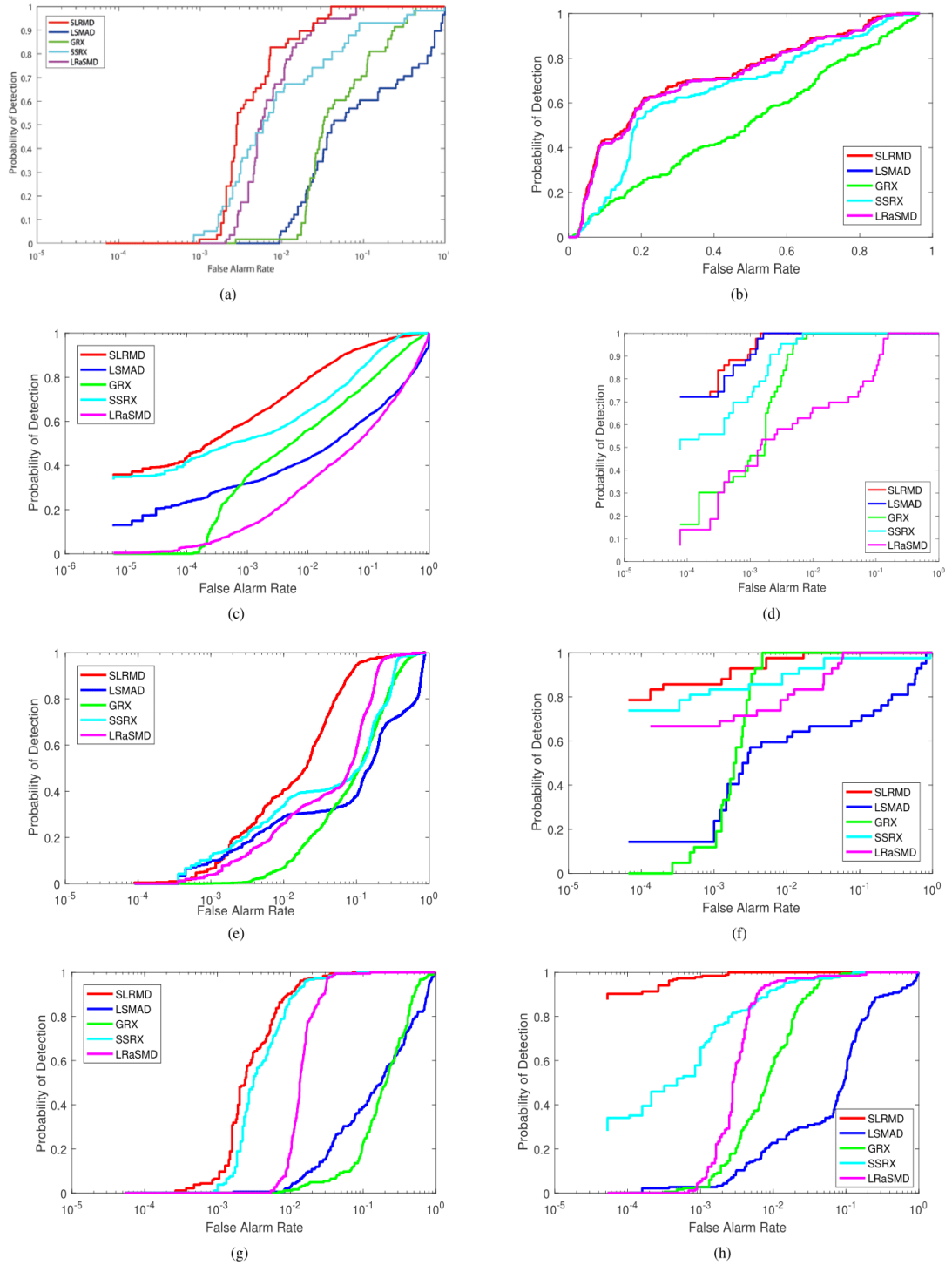


Figure 5.2 ROC curves for a) SDA subset 1. b) SDA subset 2. c) Cri d) PaviaC. e) PaviaU sample 5. f) Salinas real. g) Salinas imp4. h) Salinas imp14. i) Indian Pines sample 1. j) Indian Pines sample 2. k) Indian Pines sample 3. l) Indian Pines sample 4. m) Indian Pines sample 5. n) ABU airport 1. o) ABU airport 2. p) ABU airport 4. q) ABU urban 3. r) ABU urban 4. s) ABU urban 5.

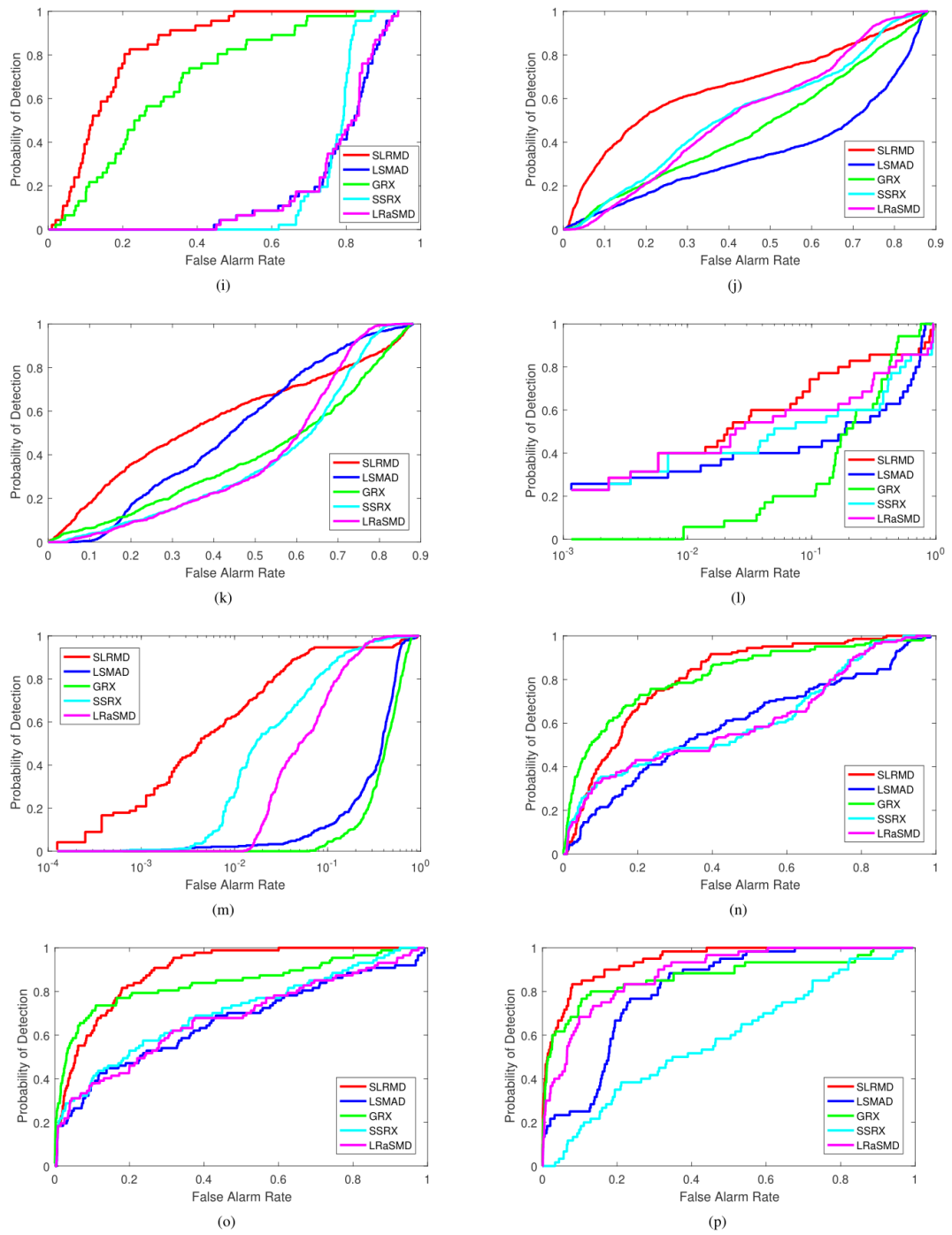


Figure 5.2 (continue) ROC curves for a) SDA subset 1. b) SDA subset 2. c) Cri d) PaviaC. e) PaviaU sample 5. f) Salinas real. g) Salinas imp4. h) Salinas imp14. i) Indian Pines sample 1. j) Indian Pines sample 2. k) Indian Pines sample 3. l) Indian Pines sample 4. m) Indian Pines sample 5. n) ABU airport 1. o) ABU airport 2. p) ABU airport 4. q) ABU urban 3. r) ABU urban 4. s) ABU urban 5.

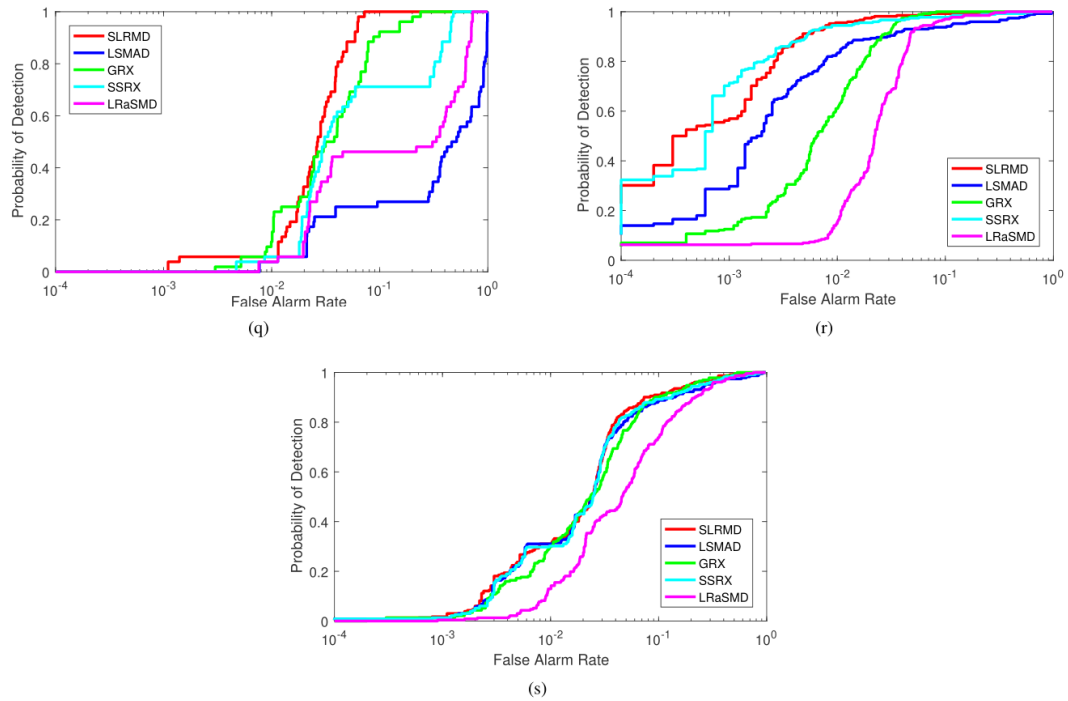


Figure 5.2 (continue) ROC curves for a) SDA subset 1. b) SDA subset 2. c) Cri d) PaviaC. e) PaviaU sample 5. f) Salinas real. g) Salinas imp4. h) Salinas imp14. i) Indian Pines sample 1. j) Indian Pines sample 2. k) Indian Pines sample 3. l) Indian Pines sample 4. m) Indian Pines sample 5. n) ABU airport 1. o) ABU airport 2. p) ABU airport 4. q) ABU urban 3. r) ABU urban 4. s) ABU urban 5.

Salinas real and synthetic results are presented in Figure 5.2 f)-h). According to real data results, proposed method is above other lines between 0.001-0.01 FAR. After middle of that point, GRX slightly passes it more Pd values. Nevertheless, SLRMD has higher performance than GRX when AUC values are considered. After 0.8 Pd, and 0.0001-0.1 FARs SLRMD, SSRX, and LRSMD plots are similar. As for imp4 data result, SLRMD and SSRX lines are closer. Yet, SLRMD line is still above all lines with higher Pd and less FAR. The result for imp14 for proposed method is distinct from the others. Its Pd values is always above 90% percent. It reaches 100% detection with less FAR.

Indian pines results are shown in Figures 5.2 i)-m). Here the materials are agricultural products: alfalfa, corn and grass. In general, SLRMD surpasses the other methods. In Figure 5.2 l), the lines are closer to each other. When Table 5.1 and Table 5.2 is considered, proposed method has higher AUC values as well. However, it is not

exceeding 85% AUC except from sample 5 which is 95%. The other methods values are between twenties and seventies percentage. Moreover, two dimensional results support the aforementioned analysis by not having a visually better look. Furthermore, the results in Table 5.2 which is constructed according to categories have the least AUC values between the other materials. We can conclude that agricultural products are not detected effectively by the other methods.

Last figures are for the ABU datasets. Figures 5.2 n), o), and p) are for ABU airport 1, 2, and 4, and the others for ABU urban 3, 4, and 5, respectively. SLRMD surpasses the other methods in airport images and urban 3 data. For airport 1 and 2, proposed method and GRX lines are closer. After 0.3 FAR in airport 1 and 0.2 FAR in airport 2 SLRMD and GRX Pd rates are going opposite sides. SLRMD's Pd rates are getting higher than GRX and the other methods as well. SLRMD and GRX performance is the most competitive in airport 1 with 82% AUC. On the contrary, it is about 90% AUC for SLRMD which is the highest for airport 2. It is followed by GRX with 84% AUC. This AUC difference is clearly seen from the Figure 5.2 o). The other methods plots are akin to each other roughly equivalent to 60% AUC for airport, and 65% AUC for airport 2. As for airport 4, SLRMD line is close to GRX until 0.6 Pd with same FARs. Nevertheless, its Pd value sharply increases up to 0.8 Pd, and, then, rises steadily until 100%Pd. Furthermore, SLRMD AUC value is the highest with 94% while the others are less than eighties.

Finally, ABU urban 3, 4, and 5 are the last three images in Figure 5.2. Proposed method's result for urban 3 data is always above other lines after 0.2 Pd and below 0.1 Pd. It detects all target pixels with FAR less than 0.1 which the lowest. For urban 4, SLRMD and SSRX results are competitive. SLRMD passes between 0.3-0.5 Pd. On the other hand, SSRX has higher Pd between 0.5-0.8 Pd. Then, they are following each other with lowest FAR than the other methods. While the most competitive methods have 99% AUC, the others are about 96%. Except from LRaSMD, the other lines draw similar plot for urban 5 data. Although their AUC values about 95%, LRaSMD has 91% AUC according to Table 5.1.

CHAPTER 6

CONCLUSION

A sparse matrix and low-rank decomposition based hyperspectral anomaly detection method is proposed in this study. It aims to find the correct separation of the high dimensional data as low-rank and sparse matrices, and to obtain anomaly locations. After the decomposition, Mahalanobis distance is applied to the sparse part of the image to get anomalous locations. The proposed method has been tested with three hyperspectral data sets. Experiments on the data sets suggest that SLRMD finds anomaly locations better. Additionally, the results denote that the proposed method outperforms other state-of-the-art methods.

Twenty hyperspectral datasets are used for evaluations: Pavia Centre, Cri, Salinas, Indian Pines, Pavia University, San Diego Airport, and Airport-Beach-Urban data. Any material in the images are chosen as a target object and images are resized. According to these new targets, new ground truths are constructed. With these new resized data and their ground truths, the methods are compared. Three datasets were used previously for comparisons in the paper: San Diego Airport, Pavia University, and Cri. According to the results shown in the ROC figures, two dimensional results, and AUC values in the tables, proposed method, SLRMD, outperforms the other anomaly detectors. For future work, the method can be extended to different data sets particularly having cluttered backgrounds.

REFERENCES

- [1] Briottet, X., Boucher, Y., Dimmeler, A., Malaplate, A., Cini, A., Diani, M., et al. Military applications of hyperspectral imagery. International Society for Optics and Photonics, Targets and backgrounds XII: Characterization and representation, 6239. 2006.
- [2] Levenson, R. M., Wachman, E. S., Niu, W., & Farkas, D. L. Spectral imaging in biomedicine: A selective overview. International Society for Optics and Photonics, Imaging Spectrometry IV, 3438, 300–313. 1998.
- [3] Harvey, A. R., Lawlor, J., McNaught, A. I., Williams, J. W., & Fletcher-Holmes, D. W. Hyperspectral imaging for the detection of retinal disease. International Society for Optics and Photonics, Imaging Spectrometry VIII, 4816, 325–336. 2002.
- [4] Manolakis, D., Lockwood, R., Cooley, T., & Jacobson, J. Is there a best hyperspectral detection algorithm? Proc.SPIE, 7334 – 16. 2009.
- [5] Nasrabadi, N. M. Hyperspectral target detection: An overview of current and future challenges. IEEE Signal Processing Magazine, 31, 34–44. 2014.
- [6] Manolakis, D. Detection algorithms for hyperspectral imaging applications: a signal processing perspective. In IEEE Workshop on Advances in Techniques for Analysis of Remotely Sensed Data, 378-384. 2003.
- [7] Manolakis, D. G. Overview of algorithms for hyperspectral target detection: theory and practice. International Society for Optics and Photonics, in Algorithms and Technologies for Multispectral, Hyperspectral, and Ultraspectral Imagery VIII, 4725, 202–216. 2002.
- [8] Matteoli, S., Diani, M., and Corsini, G. A tutorial overview of anomaly detection in hyperspectral images. IEEE Aerospace and Electronic Systems Magazine 25, 5–28. 2010.

- [9] Trigueros-Espinosa, B., V'elez-Reyes, M., Santiago, N. G., & Rosario-Torres, S. Publisher's note: Evaluation of the graphics processing unit architecture for the implementation of target detection algorithms for hyperspectral imagery. *Journal of Applied Remote Sensing*, 6(1), 060102. 2012.
- [10] Küçük, F., Töreyn, B. U., & Çelebi, F. V. Sparse and low-rank matrix decomposition-based method for hyperspectral anomaly detection. *Journal of Applied Remote Sensing*, 13(1), 014519. 2019.
- [11] Bian, X., & Krim, H. Bi-sparsity pursuit for robust subspace recovery. in *Image Processing (ICIP), 2015 IEEE International Conference on*, 3535–3539, IEEE, 2015.
- [12] Lin, Z., Liu, R., & Su, Z. Linearized alternating direction method with adaptive penalty for low-rank representation. *Advances in neural information processing systems*, 612–620. 2011.
- [13] Cand`es, E. J., Li, X., Ma, Y., & Wright, J. Robust principal component analysis? *J. ACM* 58, 11:1–11:37. 2011.
- [14] Liu, G., Lin, Z., Yan, S., Sun, J., Yu, Y., & Ma, Y. Robust recovery of subspace structures by low-rank representation. *IEEE Transactions on Pattern Analysis and Machine Intelligence* 35, 171–184. 2013.
- [15] Elhamifar, E., & Vidal, R. Sparse subspace clustering: Algorithm, theory, and applications. *IEEE Transactions on Pattern Analysis and Machine Intelligence* 35(11), 2765 – 2781. 2013.
- [16] Chen, S.-Y., Yang, S., Kalpakis, K., & Chang, C. I. Low-rank decomposition-based anomaly detection. *Proc.SPIE* 8743, 8743 – 8743 – 7. 2013.
- [17] Küçük, F., Töreyn, B. U., & Çelebi, F. V. Anomaly detection in hyperspectral data with matrix decomposition. *IEEE, 26th Signal Processing and Communications Applications Conference (SIU)*, (pp. 1-4). 2018.

- [18] Elhamifar, E., Sapiro, G., & Vidal, R. See all by looking at a few: Sparse modeling for finding representative objects. *IEEE, Conference on Computer Vision and Pattern Recognition*, 1600–1607. 2012.
- [19] Li, J., Zhang, H., Zhang, L. & Ma, L. Hyperspectral anomaly detection by the use of background joint sparse representation. *IEEE Journal of Selected Topics in Applied Earth Observations and Remote Sensing* 8, 2523–2533. 2015.
- [20] Ramirez, I., Sprechmann, P., & Sapiro, G. Classification and clustering via dictionary learning with structured incoherence and shared features. *IEEE Computer Society Conference on Computer Vision and Pattern Recognition*, 3501–3508. 2010.
- [21] Chen, Y., Nasrabadi, N. M., & Tran, T. D. Hyperspectral image classification using dictionary-based sparse representation. *IEEE Transactions on Geoscience and Remote Sensing* 49, 3973–3985. 2011.
- [22] Lin, Z., Chen, M., & Ma, Y. The augmented lagrange multiplier method for exact recovery of corrupted low-rank matrices. *CoRR*, 1009.5055. 2009.
- [23] Goetz, A. F., Vane, G., Solomon, J. E. & Rock, B. N. Imaging spectrometry for earth remote sensing. *Science* 228(4704), 1147–1153. 1985.
- [24] Manolakis, D., & Shaw, G. Detection algorithms for hyperspectral imaging applications. *IEEE Signal Processing Magazine* 19, 29–432. 2002.
- [25] Rashmi, S., Addamani, S., & Ravikiran, A. Spectral Angle Mapper Algorithm for Remote Sensing Image Classification. *IJISSET–International Journal of Innovative Science, Engineering & Technology* 50.4:201-205. 2014.
- [26] Harsanyi, J.C. & Chang, C.I. Detection of low probability subpixel targets in hyperspectral image sequences with unknown backgrounds. *IEEE Transactions on Geoscience and Remote Sensing*, vol. 32, pp. 779-785. 1994.

- [27] Harsanyi, J. C. Detection and classification of subpixel spectral signatures in hyperspectral image sequences. Ph.D. dissertation, Dept. Elect. Eng., Univ. Maryland Baltimore County, Baltimore, MD. 1993.
- [28] Ayoub, T. F. & Haimovich, A. R. Modified GLRT signal detection algorithm. IEEE Transactions on Aerospace and Electronic Systems, 36(3), 810-818. 2000.
- [29] McWhorter, L. T., Scharf, L. L. & Griffiths, L. J. Adaptive coherence estimation for radar signal processing. IEEE Signals, Systems and Computers, Conference Record of the Thirtieth Asilomar Conference on (Vol. 1, pp. 536-540). 1996.
- [30] Gao, L., Yang, B., Du, Q., & Zhang, B. Adjusted spectral matched filter for target detection in hyperspectral imagery. Remote Sensing 7.6, 6611-6634. 2015.
- [31] Jin, X., Paswaters, S., & Cline, H. A comparative study of target detection algorithms for hyperspectral imagery. SPIE Defense, Security, and Sensing International Society for Optics and Photonics, Vol. 7334, p. 73341. 2009.
- [32] Du, Q., Ren, H., & Chang, C. I. A comparative study for orthogonal subspace projection and constrained energy minimization. IEEE Transactions on Geoscience and Remote Sensing, 41(6), 1525-1529. 2003.
- [33] Richmond, C. D. Performance of the adaptive side lobe blanker detection algorithm in homogeneous environments. IEEE Transactions on Signal Processing, 48(5), 1235-1247. 2000.
- [34] Ward, J. *Space-time adaptive processing for airborne radar*. IEE Colloquium on Space-Time Adaptive Processing, 1998.
- [35] Manolakis, D., Marden, D., & Shaw, G. A. Hyperspectral image processing for automatic target detection applications. Lincoln laboratory journal, 14(1), 79-116. 2003.
- [36] Kwon, H. & Nasrabadi, N. M. A comparative analysis of kernel subspace target detectors for hyperspectral imagery. EURASIP Journal on Advances in Signal Processing, 2007(1), 029250. 2006.

- [37] Kwon, H. & Nasrabadi, N. M. Kernel orthogonal subspace projection for hyperspectral signal classification. *IEEE Transactions on Geoscience and Remote Sensing*, 43(12), 2952-2962. 2005.
- [38] Kwon, H. & Nasrabadi, N. M. Kernel adaptive subspace detector for hyperspectral imagery. *IEEE Geoscience and Remote Sensing Letters*, 3(2), 271-275. 2006.
- [39] Salem, M.B., Ettabaa, K. S. & Hamdi, M.A. Anomaly detection in hyperspectral imagery: an overview. *IEEE International Image Processing, Applications and Systems Conference*, (pp. 1-6). 2014.
- [40] Zhang, Y., Du, B., Zhang, L., & Wang, S. A Low-Rank and Sparse Matrix Decomposition-Based Mahalanobis Distance Method for Hyperspectral Anomaly Detection. *IEEE Transactions on Geoscience and Remote Sensing*, 54(3), 1376-1389. 2016.
- [41] Borengasser, M., Hungate, W. S., & Watkins, R. *Hyperspectral remote sensing: principles and applications*. CRC press. 2007.
- [42] Reed, I. S. & Yu, X. Adaptive multiple-band cfar detection of an optical pattern with unknown spectral distribution. *Acoustics, Speech and Signal Processing, IEEE Trans. on*, vol. 38, no. 10, pp. 1760–1770. 1990.
- [43] Zhao, R., Du, B., & Zhang, L. A robust nonlinear hyperspectral anomaly detection approach. *IEEE Journal of Selected Topics in Applied Earth Observations and Remote Sensing*, 7(4), 1227-1234. 2014.
- [44] Du, B., & Zhang, L. Random-selection-based anomaly detector for hyperspectral imagery. *IEEE Transactions on Geoscience and Remote sensing*, 49(5), 1578-1589. 2011.
- [45] Chang, C. I. Target signature-constrained mixed pixel classification for hyperspectral imagery. *IEEE transactions on geoscience and remote sensing*, 40(5), 1065-1081. 2002.

- [46] Kwon, H. & Nasrabadi, N. M. Kernel RX-algorithm: A nonlinear anomaly detector for hyperspectral imagery. *IEEE Transactions on Geoscience and Remote Sensing*, 43(2), 388-397. 2005.
- [47] Kwon, H. & Nasrabadi, N.M. Kernel adaptive subspace detector for hyperspectral target detection. *IEEE International Conference on Acoustics, Speech, and Signal Processing, (ICASSP '05)*, Vol. 4, pp. iv/681-iv/684. 2005.
- [48] Banerjee, A., Burlina, P., & Diehl, C. A support vector method for anomaly detection in hyperspectral imagery. *IEEE Transactions on Geoscience and Remote Sensing*, 44(8), 2282. 2006.
- [49] Carlotto, M.J. A Cluster-Based Approach for Detecting Man-Made Objects and Changes in Imagery. *IEEE Transactions on Geoscience and Remote Sensing*, Vol. 43, no. 2, pp. 374-387. 2005.
- [50] Kim, D. H. & Finkel, L. H. Hyperspectral Image Processing Using Locally Linear Embedding. *IEEE EMBS Conference on Neural Engineering*, Italy, pp. 316 – 319. 2003.
- [51] W. Sun, C. Liu, J. Li. Low-rank and sparse matrix decomposition-based anomaly detection for hyperspectral imagery. *Journal of Applied Remote Sensing* 8(1), 083641–083641. 2014.
- [52] Zhou, T. & Tao, D. Godec: Randomized low-rank & sparse matrix decomposition in noisy case. *International conference on machine learning*, Omnipress, 2011.
- [53] Chang, H., Wang, T., Li, A., & Fang, H. Local hyperspectral anomaly detection method based on low-rank and sparse matrix decomposition”, *Journal of Applied Remote Sensing*, 13(2), 026513. 2019.
- [54] Zhou, T., & Tao, D. Bilateral random projections. *IEEE International Symposium on Information Theory Proceedings* (pp. 1286-1290). 2012.

- [55] Yang, Y., Zhang, J., Song, S., Zhang, C., & Liu, D. Low-Rank and Sparse Matrix Decomposition with Orthogonal Subspace Projection-Based Background Suppression for Hyperspectral Anomaly Detection. *IEEE Geoscience and Remote Sensing Letters*, 2019.
- [56] Xu, Y., Wu, Z., Li, J., Plaza, A., & Wei, Z. Anomaly detection in hyperspectral images based on low-rank and sparse representation. *IEEE Transactions on Geoscience and Remote Sensing*, 54(4), 1990-2000. 2016.
- [57] Cheng, T., & Wang, B. Graph and Total Variation Regularized Low-Rank Representation for Hyperspectral Anomaly Detection. *IEEE Transactions on Geoscience and Remote Sensing*, 2019.
- [58] Khazai, S., Homayouni, S. & Safari, A. Anomaly detection in hyperspectral images based on an adaptive support vector method. *IEEE Geoscience and Remote Sensing Letters* 8, 646–650. 2011.
- [59] Bian, X. & Krim, H. Robust subspace recovery via bi-sparsity pursuit. *arXiv preprint arXiv:1403.8067*. 2014.
- [60] Elhamifar, E. & Vidal, R. Sparse subspace clustering. *IEEE Computer Vision and Pattern Recognition, CVPR, IEEE Conference on*, 2790–2797. 2009.
- [61] Rockafellar, R. T. Augmented lagrange multiplier functions and duality in nonconvex programming. *SIAM Journal on Control* 12(2), 268–285. 1974.
- [62] Manolakis, D., Rossacci, M., Zhang, D. Statistical characterization of hyperspectral background clutter in the reflective spectral region. *Appl. Opt.* 47, F96–F106. 2008.
- [63] Carlotto, M. J. A cluster-based approach for detecting man-made objects and changes in imagery. *IEEE Trans. Geosci. Remote Sens.* 43, 374–387. 2005.
- [64] Kozoderov, V. V. & Dmitriev, E. V. Testing different classification methods in airborne hyperspectral imagery processing. *Optics express* 24, A956–A965. 2016.

- [65] Vafadar, M., & Ghassemian, H. Hyperspectral anomaly detection using combined similarity criteria. *IEEE Journal of Selected Topics in Applied Earth Observations and Remote Sensing*, 11(11), 4076-4085. 2018.
- [66] Bioucas-Dias, J. M. & Nascimento, J. M. P. Hyperspectral subspace identification. *IEEE Transactions on Geoscience and Remote Sensing* 46, 2435–2445. 2008.
- [67] Green, R. O., Eastwood, M. L., Sarture, C. M. Imaging spectroscopy and the airborne visible/infrared imaging spectrometer (AVIRIS). *Remote Sens. Environ.* 65, 227–248.1998.
- [68] Vafadar, M., & Ghassemian, H. Anomaly detection of hyperspectral imagery using modified collaborative representation. *IEEE Geoscience and Remote Sensing Letters*, 15(4), 577-581.2018.
- [69] Kunkel, B., Blechinger, F., Lutz, R. RosiS (reflective optics system imaging spectrometer) - a candidate instrument for polar platform missions. *ROSIS (Reflective Optics System Imaging Spectrometer) - A Candidate Instrument For Polar Platform Missions, Proc.SPIE 0868*, 0868 – 0868 – 8. 1988.
- [70] Pavia Centre Hyperspectral dataset. Retrieved February 20, 2017, from http://www.ehu.es/ccwintco/index.php/Hyperspectral_Remote_Sensing_Scenes#Pavia_Centre_scene
- [71] Goetz, A.F., Vane, G., Solomon, J.E., Rock, B.N. Imaging spectrometry for Earth remote sensing. *Science*, 228, 1147–1153. 1985.
- [72] Pavia University hyperspectral dataset. Retrieved February 20, 2017, from http://www.ehu.es/ccwintco/index.php/Hyperspectral_Remote_Sensing_Scenes#Pavia_University_scene
- [73] Salinas hyperspectral dataset. Retrieved February 20, 2017, from http://www.ehu.es/ccwintco/index.php/Hyperspectral_Remote_Sensing_Scenes#Salinas

- [74] Verdoja, F., & Grangetto, M. Graph Laplacian for Image Anomaly Detection. arXiv preprint arXiv:1802.09843. 2018.
- [75] Chang, C.I., Chiang, S.S. Anomaly detection and classification for hyperspectral imagery. *IEEE Transactions on Geoscience and Remote Sensing* 40(6), 1314–1325. 2002.
- [76] Indian pines hyperspectral dataset. Retrieved February 20, 2017, from http://www.ehu.eus/ccwintco/index.php/Hyperspectral_Remote_Sensing_Scenes#Indian_Pines
- [77] London, A. L. & Shah, R. K. Offset Rectangular Plate-fin Surfaces-Heat Transfer and Flow Friction Characteristics. *ASME J. Eng. Power*, 90(3), 218-228. 1968.
- [78] Xudong Kang. ABU hyperspectral datasets. Retrieved January 10, 2018, from <http://xudongkang.weebly.com/data-sets.html>
- [79] Chang, C. I. Multiparameter receiver operating characteristic analysis for signal detection and classification. *IEEE Sens. J.* 10, 423–442. 2010.
- [80] Parker, D. R., Gustafson, S. C., & Ross, T. D. Receiver operating characteristic and confidence error metrics for assessing the performance of automatic target recognition systems. *Opt. Eng.* 44, 097202. 2005.